Engineering Fracture Mechanics 246 (2021) 107627

Contents lists available at ScienceDirect

Engineering Fracture Mechanics

journal homepage: www.elsevier.com/locate/engfracmech

Cohesive fracture model of rocks based on multi-scale model and Lennard-Jones potential

Qindong Lin [a,b], Shihai Li [a,b], Chun Feng [a,*], Xinquan Wang [a,b]

[a] Key Laboratory for Mechanics in Fluid Solid Coupling Systems, Institute of Mechanics, Chinese Academy of Sciences, Beijing 100190, China
[b] School of Engineering Science, University of Chinese Academy of Sciences, Beijing 100049, China

ARTICLE INFO

Keywords:
Multi-scale model
Lennard-Jones potential
Cohesive fracture model
Fracture energy

ABSTRACT

With the aim of modelling the energy dissipation phenomenon during the initiation and propagation of cracks, a novel cohesive fracture model is proposed in this study based on the multi-scale model of rocks and the Lennard-Jones potential between non-bonding molecules. The proposed model establishes the corresponding relationship of deformation in the multi-scale model of rocks and suggests that the fracture energy is essentially the manifestation of the transformation of deformation energy into potential energy between molecules. First, the multi-scale model of rocks is established based on the structural characteristics and fracture characteristics of rocks, and the corresponding relation of deformation at different scales is analysed. Thereafter, the force and potential energy equations of the cohesive fracture model corresponding to the tensile and shear processes are established. Finally, the accuracy of the cohesive fracture model is verified through three numerical simulations. The results indicate that the cohesive fracture model can accurately fit the theoretical values and experimental results in the Mode-I and Mode-II tests. In the uniaxial compression test, the cohesive fracture model can accurately simulate the uniaxial compressive strength and fracture pattern of rocks.

1. Introduction

Rocks, naturally formed by a long-term geological action, may be composed of cementing substances, mineral particles, and pores. Because rocks are abundantly found close to tunnels, mines, and slopes, scholars have conducted extensive research on the failure process of rocks [1–7]. Laboratory tests, theoretical analysis, and numerical simulation are the main methods to study the failure process of rocks. Based on the results of the laboratory tests on rocks, researchers have concluded that rocks exhibit complex constitutive characteristics and that the failure process of a rock is progressive under the action of an external load [8–10]. In addition, part of the deformation energy is dissipated during the initiation and propagation of cracks. Because acoustic emission (AE) has the advantages of dynamic real-time monitoring, non-destructive monitoring, and easy calibration of the damage position, AE has been widely used to obtain the crack information (for example: crack position and number of cracks) of rocks in laboratory tests [11–15]. To describe the complex constitutive characteristics of rocks more accurately, several scholars have proposed various theoretical constitutive models of rocks based on several theories (for example, statistical damage theory) [16–20].

With the rapid development of computer technology, many numerical simulation methods have been proposed to study the failure process of rocks. Because the basic theories of numerical simulation methods are different, these methods can be categorised into

* Corresponding author.
E-mail address: fengchun@imech.ac.cn (C. Feng).

https://doi.org/10.1016/j.engfracmech.2021.107627
Received 11 September 2020; Received in revised form 9 January 2021; Accepted 21 February 2021
Available online 24 February 2021

Nomenclature

w_{lj}	Lennard-Jones (L-J) potential
r	distance between two molecules
ε_0	depth of the L-J potential well
r_0	distance at which the L-J potential is zero
F_{vd}	van der Waals force
r_e	distance at which the L-J potential reaches the minimum
r_s	distance at which F_{vd} reaches the maximum
r_d	distance at which F_{vd} is zero
β	thickness ratio
ω	space occupancy ratio
S_{am}	boundary area occupied by molecules in actual model
S_a	boundary area in actual model
S_{tm}	boundary area occupied by molecules in theoretical model
S_t	boundary area in theoretical model
λ	contact ratio
G_{fI}	tensile fracture energy
G_{fII}	shear fracture energy
F_L	external load
N_f^t	number of molecules between adjacent layers during tensile process
s_m	area of a molecule
W_t	tensile potential energy of rupture field
F_t	tensile force of rupture field
W_s	shear potential energy of rupture field
F_s	shear force of rupture field
N_f^s	number of molecules between adjacent layers during shear process
Δr_v	increase in the normal distance
Δr_u	increase in the tangential distance
σ_t	tensile strength
α	crack ratio
S_c	area of the cracked interface
S_e	area of the entire interface
R	specimen radius
S	distance between support points
a_0	initial crack length
t	initial crack width
σ_s	shear stress
σ_n	normal stress
$\ddot{\boldsymbol{u}}(t)$	acceleration vector
$\dot{\boldsymbol{u}}(t)$	velocity vector
$\boldsymbol{u}(t)$	displacement vector
$\boldsymbol{M}$	mass matrix
$\boldsymbol{C}$	damping matrix
$\boldsymbol{K}$	stiffness matrix
$\boldsymbol{F}(t)$	vector of the external force
$\Delta\sigma_{ij}$	element stress increment
$\Delta\varepsilon_{ij}$	element strain increment
$\Delta\theta$	element bulk strain increment
K	bulk modulus
G	shear modulus
δ_{ij}	Kronecker symbol
σ_{ij}	element trial stress
$\sigma_{ij\text{-}old}$	element stress at the last time-step

continuum-based methods (such as finite element method (FEM) [21,22], boundary element method (BEM) [23,24], finite volume method (FVM) [25,26], cracking elements method (CEM) [27–29], and peridynamics (PD) [30–32]), discontinuum-based methods (such as discrete element method (DEM) [33–35], extended finite element method (XFEM) [36,37], and discontinuous deformation analysis (DDA) [38,39]), mesh-free methods (for example, smoothed particle hydrodynamics (SPH) [40,41], general particle dynamics

(GPD) [42,43], cracking particle method (CPM) [44,45]) and coupled methods (such as FEM/DEM, FEM/DDA, and FEM/SPH) [46–50]. Based on these numerical simulation methods, scholars have conducted extensive analyses of the rock fracture process under different conditions [51–54].

To describe the initiation and propagation of cracks more accurately as well as characterise the fracture energy via numerical simulation, scholars have proposed several fracture models of rocks. Owing to its advantages of comprehensive theoretical knowledge, clear mechanical meaning, and convenience of implementation, the cohesive fracture model has attracted the attention of many scholars, and has been widely used to simulate the initiation and propagation of cracks in rocks. The cohesive fracture model was first proposed by Barenblatt (1959) and Dugdale (1960); Hillerborg et al. (1976) proposed the fictitious crack model that realises the simulation of the energy dissipation process during the fracture process [55–57]. In the cohesive fracture model, a rock is regarded as the assemblage of solid elements that are connected by the cohesive interface elements at the common boundaries. The cohesive interface elements provide the potential space for crack initiation and propagation, and they are assumed to be considerably thin. Based on the early theoretical knowledge, scholars have invested extensive efforts into developing the cohesive fracture model. To investigate the softening behaviour, several theoretical softening laws have been proposed, including bilinear, linear-parabolic, exponential, and trapezoidal [58].

Many scholars have studied the fracture process of rocks and rock-like materials based on the cohesive fracture model. Based on the cohesive crack propagation, Gálvez et al. [59] developed a numerical procedure for mixed-mode fracture of quasi-brittle materials, and found that the numerical results agreed well with the experimental results. To represent the random heterogeneous fracture properties, Yang et al. [60] developed a numerical method, wherein the potential cracks are represented by cohesive elements modelled by spatially varying the Weibull random fields. Wu et al. [61] established a user-defined material model with stochastic strengths to correspond to the cohesive fracture model, and the heterogeneity effect on the dynamic failure process and dynamic strength was studied. Zhou et al. [62] proposed the constitutive law of the rate-dependent cohesive model and verified the accuracy of the model by comparing the results with the experimental data obtained from the spall tests. Gui et al. [63] proposed a cohesive fracture model that could represent the tension, compression, and shear material behaviour, and three numerical simulations were conducted to verify the accuracy of the model. By introducing the mixed-mode cohesive traction response, Jiang et al. [64] investigated the rock fracture, penetration force, and chip shape during rock breaking using a conical pick. Nguyen et al. [65] established a novel cohesive model coupling damage mechanics based on the plasticity theory to characterise the failure mechanism of cement bridges, and they studied the influence of specimen geometries on the fracture toughness in a semi-circular bending test. The cohesive fracture model enables scholars to understand the fracture process of rocks extensively.

However, the current research on the rock fracture process has two main limitations. First, the theoretical analysis conducted to study the energy dissipation mechanism during the initiation and propagation process of cracks, is insufficient. Second, although several cohesive fracture models have been proposed, in the most commonly used model, it is generally considered that the cohesive force decreases linearly as the crack opening displacement increases in the softening stage, and the cohesive force increases linearly as the crack opening displacement increases before the cohesive force reaches the maximum value. The underlying reason for this changing trend is not appropriately discussed.

Based on the multi-scale model of rocks and the Lennard-Jones potential between non-bonding molecules, this study aims to investigate the energy dissipation mechanism during the initiation and propagation process of cracks and establish the force and potential energy equations for the novel cohesive fracture model.

The rest of this paper is organised as follows. In Section 2, the multi-scale model of rocks and the Lennard-Jones potential are introduced, and some key parameters are defined. In Section 3, the force and potential energy equations of the novel cohesive fracture model in the tensile and shear processes are established. In Section 4, the accuracy of the cohesive fracture model is verified through three numerical simulations, namely Mode-I test, Mode-II test, and uniaxial compression test.

2. Theoretical background

2.1. Lennard-Jones potential

The neutral molecules are subjected to two different forces within the short-distance and long- distance ranges: an attractive force at a long distance and a repulsive force at a short distance. The Lennard-Jones potential proposed by John Lennard-Jones represents a simple mathematical model that describes the potential energy of the interaction between two non-bonding molecules based on the separation distance. The formula is shown in Eq. (1), wherein the term $(\frac{1}{r})^{12}$ denotes the repulsive force and the term $(\frac{1}{r})^{6}$ denotes the attractive force.

$$w_{lj} = 4\varepsilon_0[(\frac{r_0}{r})^{12} - (\frac{r_0}{r})^{6}] \tag{1}$$

where w_{lj} denotes the Lennard-Jones potential between two non-bonding molecules, r denotes the separation distance between two non-bonding molecules, ε_0 denotes the depth of the potential well and a measure of the strength of the attractive force between the two molecules, and r_0 denotes the finite distance at which the intermolecular potential energy between two non-bonding molecules is zero.

The van der Waals force is equal to the negative gradient value of the Lennard-Jones potential, and is represented by the following equation:

$$F_{vd} = -\frac{dw_{lj}}{dr} = \frac{24\varepsilon_0}{r_0}\left[\frac{2r_0^{13}}{r^{13}} - \frac{r_0^7}{r^7}\right] \tag{2}$$

The curves corresponding to the change in the Lennard-Jones potential w_{lj} and van der Waals force F_{vd} are plotted in Fig. 1. It can be observed that the repulsive force dominates at a short distance, whereas the attractive force dominates at a long distance. Based on the changing trends of w_{lj} and F_{vd}, it can be observed that there are several eigen values of r. When $r = r_0$, the Lennard-Jones potential w_{lj} is equal to zero. When $r = r_e$, the van der Waals force F_{vd} is equal to zero, and the Lennard-Jones potential w_{lj} attains the minimum value w_{min}. When $r = r_s$, the van der Waals force F_{vd} attains the maximum value F_{max}. When $r = r_d$, it is regarded that there is no interaction between two non-bonding molecules, and the Lennard-Jones potential w_{lj} and van der Waals force F_{vd} are equal to zero; $r_e = \sqrt[6]{2}r_0$, $r_s = \sqrt[6]{\frac{26}{7}}r_0$, and $r_d = 5r_0$.

2.2. Multi-scale model

As an important model in mechanical analysis, the representative volume element (RVE) is characterised by being "infinity small at the macro-scale, and infinity large at the micro-scale". Therefore, it can characterise both the complex mechanical characteristics as well as the complex structural characteristics of rocks. The initiation and propagation process of cracks in a rock under an external load is plotted in Fig. 2. From Fig. 2(a), it can be observed that the RVE of the rock is composed of mineral particles, cementing substances, and pores. Initially, during loading, no crack occurs because the stress is small. As the loading duration increases, the stress gradually increases, and some cracks (denoted by the red solid lines) gradually appear at certain regions with a weak bearing strength (as depicted in Fig. 2(b)). Because the strength of a mineral particle is considerably stronger than that of a cementing substance, cracks mainly occur at the cementing substance between the mineral particles [66]. With the continuous increase in stress, the cracks gradually propagate, and eventually, a penetrative crack appears in the RVE (Fig. 2(c)). In the initiation and propagation process of cracks, the deformation energy is partially dissipated, which is defined as the fracture energy.

In comparison with the size of the RVE, the size of the crack is significantly small. Therefore, based on the structural characteristics and fracture characteristics of rocks, a multi-scale model of rocks, composed of RVE scale, particle scale, and molecular scale, is proposed to study the energy dissipation mechanism.

RVE scale is the basic scale for describing the complex mechanical characteristics and structural characteristics of rocks. However, the initiation and propagation process of cracks and energy dissipation mechanism cannot be studied at this scale.

Particle scale is the basic scale for describing the initiation and propagation process of cracks. Pores, cementing substances, and mineral particles coexist at this scale, and cracks occur at the cementing substance between the mineral particles. The bearing strength of the RVE scale can be reflected by this scale; however, the energy dissipation mechanism cannot be studied at this scale.

Molecular scale is the basic scale for studying the energy dissipation mechanism. It is assumed that the cementing substance between the mineral particles is composed of a large number of non-bonding molecules. The potential energy between the molecules can be described as the Lennard-Jones potential, and the force between the molecules can be described as the van der Waals force.

In the multi-scale model of rocks, each scale represents the different characteristics of rocks. The RVE scale describes the complex mechanical characteristics and structural characteristics of rocks. The particle scale describes the initiation and propagation process of cracks in the rocks. The molecular scale describes the energy dissipation mechanism in the initiation and propagation process of cracks.

From Fig. 2, it can be observed that there are no cracks in the rocks initially during loading, implying that some mechanical quantities (for example, displacement) are continuously distributed. Therefore, the rock without cracks can be regarded as a continuous medium. With the initiation of microcracks and the appearance of penetrative cracks, the rock presents obvious discontinuous characteristics, and the rock with cracks can be regarded as the discontinuous medium. Therefore, it can be determined that the rock changes from a continuous medium to a discontinuous medium during the initiation and propagation process of cracks. Based on the multi-scale model and fracture process of rocks, it is proposed that the study field is composed of continuous and rupture fields. There exist no cracks in the continuous field, and the mechanical quantities remain continuous. The space occupied by cracks in the

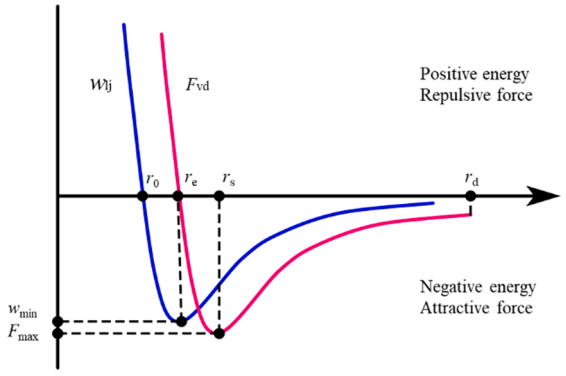

Fig. 1. Curves corresponding to the change in the Lennard-Jones potential w_{lj} and van der Waals force F_{vd}.

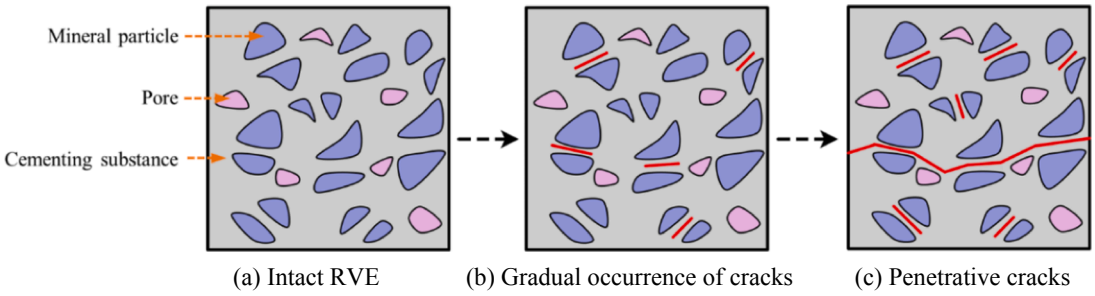

Fig. 2. Initiation and propagation process of cracks.

rock represents the rupture field, and the deformation energy is dissipated in this field. Because the opening displacement of cracks is considerably small, the rupture field can be regarded as infinitely small in comparison with the continuous field.

The schematic diagrams of the continuous and rupture fields are plotted in Fig. 3. In Fig. 3(a), the grey area indicates the continuous field, and the blue line indicates the rupture field. The local schematic diagram of the rupture field (that is, the actual model of the rupture field) is plotted in Fig. 3(b). It can be observed that there is a crack (denoted by the red line) in the rupture field, and the crack opening displacement can be regarded as infinitely small. Based on the microstructure of the rock, it can be determined that the crack exists at the cementing substance. Therefore, it is assumed that the rupture field includes crack and cementing substances on both sides of the cracks. In addition, it can be observed that the crack in the rupture field is not continuous due to the existence of pores. To simplify the theoretical analysis, only the cementing substance within a certain thickness on both sides of the cracks is selected to establish the theoretical model of the rupture field, as illustrated in Fig. 3(c).

Based on the multi-scale model of the rock and the theoretical model of the rupture field, the variations in the force and potential energy in the rupture field are studied theoretically. Three basic hypotheses are proposed first.

(1) The cementing substance of the rupture field at the particle scale is considered to be composed of a large number of neutral molecules at the molecular scale. The intermolecular potential energy can be defined as the Lennard-Jones potential, and the intermolecular force can be defined as the van der Waals force. In addition, the molecules are not closely arranged at the rupture field boundary.
(2) Based on the characteristic of the Lennard-Jones potential, it is proposed that the breakage between the molecules at the molecular scale can be determined based on the intermolecular distance. Once the intermolecular distance reaches r_d, a breakage between the molecules occurs, and the intermolecular potential energy and force become zero.
(3) There exists no shear force between the molecules at the molecular scale; therefore, the tensile strength and shear strength between the particles at the particle scale are both produced by the van der Waals force between the molecules at the molecular scale.

The corresponding relation of deformation in the multi-scale model of the rock is plotted in Fig. 4. When the external load F_L is applied at the boundary of the RVE, deformation occurs at any position in the RVE. The deformation at the RVE scale causes an increase in the distance between the mineral particles (denoted by the red dotted line in Fig. 4(a)), and it is determined that the increase in the distance between the mineral particles is equal to the strain at the RVE scale multiplied by the initial distance between the mineral particles. In addition, the bearing strength of the particle contact surface at the particle scale is closely related to the bearing strength at the RVE scale. Because there exists a cementing substance between the mineral particles, with the increase in the distance between the mineral particles, the cementing substance deforms and prevents the particles from separating. Based on the basic hypothesis 1 mentioned above, it can be concluded that the separation of mineral particles at the particle scale results in an increase in the

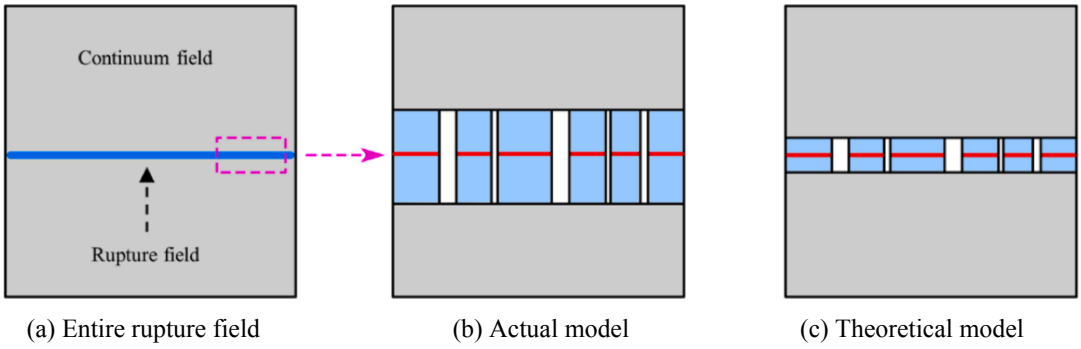

Fig. 3. Schematic diagram of continuous field and rupture field.

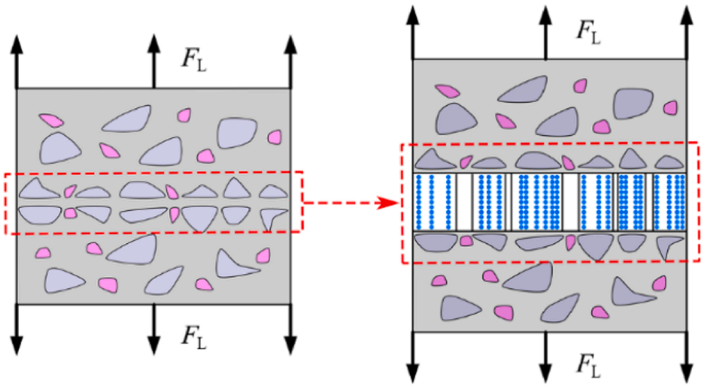

Fig. 4. Corresponding relation of deformation in multi-scale model.

intermolecular distance at the molecule scale. Moreover, the increase in the distance between the mineral particles at the particle scale is equal to the cumulative value of the increase in the intermolecular distance at the molecular scale. Once the intermolecular distance reaches r_d, the breakage between the molecules occurs, indicating the occurrence of cracks. As a result, the rupture field is observed, and the rock changes from a continuous medium to a discontinuous medium.

In addition, it is known that the potential energy between the molecules is at its minimum at the initial loading. As the deformation of the cementing substance between the mineral particles increases at the particle scale, the intermolecular distance increases at the molecular scale, causing an increase in the potential energy between the molecules. When a crack occurs, the potential energy between the molecules reaches its maximum. Therefore, based on the multi-scale model of the rock, it can be concluded that the deformation energy of the continuous field is partially transformed into the potential energy between the molecules in the rupture field, and the increase in the potential energy is equal to the fracture energy.

Based on the analysis of deformation in the multi-scale model of the rock, three important conclusions are drawn:

(1) The increase in the distance between the mineral particles is equal to the strain at the RVE scale multiplied by the initial distance between the mineral particles.
(2) The increase in the distance between the mineral particles at the particle scale is equal to the cumulative value of the increase in the intermolecular distance at the molecular scale.
(3) The essence of fracture energy is the transformation of the deformation energy of the continuous field into the potential energy between the molecules in the rupture field.

2.3. Key parameters

To establish the force expression and potential energy expression of the rupture field, certain key parameters are first defined.

2.3.1. Thickness ratio β

In the actual model of the rupture field, it is assumed that the rupture field includes cracks and cementing substances on both sides of the cracks. In contrast, in the theoretical model, to simplify the theoretical analysis, it is assumed that the rupture field includes cracks and cementing substances within a certain thickness on both sides of the cracks. Therefore, it can be observed that the thickness of the cementing substance in the actual model of the rupture field is greater than that in the theoretical model of the rupture field. The thickness of the cementing substance in the actual model is defined as H_a, and the thickness of the cementing substance in the theoretical model is defined as H_t. According to the Lennard-Jones potential characteristic, it is assumed that the cementing substance of the rupture field is composed of 11 molecular layers in the theoretical model. However, the number of molecular layers contained in the cementing substance of the rupture field should be larger than 11 in the actual model. To quantify the corresponding relationship between H_a and H_t, the thickness ratio β, a dimensionless index, is proposed, and is written as follows:

$$\beta = \frac{H_a}{H_t} \tag{3}$$

Because it is assumed that the thickness ratio of the cementing substance is equal to the number ratio of molecular layers contained in the cementing substance, the number of molecular layers in the actual model of the rupture field is equal to 11β.

2.3.2. Space occupancy ratio ω

In both the actual model and theoretical model of the rupture field, the boundary area of the rupture field includes the area of the pores and the area of the cementing substance. Because the molecules are not closely arranged at the rupture field boundary, the area

actually occupied by the molecules at the rupture field boundary is not equal to the entire boundary area of the rupture field. To characterise the boundary area actually occupied by the molecules, the space occupancy ratio ω is proposed, and is expressed as follows:

$$\omega = \frac{S_{am}}{S_a} = \frac{S_{tm}}{S_t} \tag{4}$$

where S_{am} denotes the boundary area occupied by the molecules in the actual model, S_{tm} denotes the boundary area occupied by the molecules in the theoretical model, S_a denotes the boundary area of the rupture field in the actual model, and S_t denotes the boundary area of the rupture field in the theoretical model.

Once the value of ω is known, the boundary area actually occupied by the molecules (S_{am} and S_{tm}) can be obtained.

2.3.3. Contact ratio λ

For two adjacent molecular layers at the molecular scale, it can be determined that the number of molecules possessing intermolecular force is equal to the number of molecules in the molecular layer during the tensile process. However, owing to the tangential change in the spatial position during the shear process, new intermolecular forces may be experienced by the molecules that did not originally possess intermolecular forces. Therefore, contact ratio λ is proposed to quantify the increase in the number of molecules possessing intermolecular force during the shear process. λ is determined by the shear fracture energy G_{fII} and tensile fracture energy G_{fI}, and is defined as follows:

$$\lambda = \frac{G_{fII}}{G_{fI}} \tag{5}$$

3. Methodology

In this section, the force and potential energy equations are established during the tensile process and shear process, respectively, based on the change in the molecular distance at the molecular scale.

3.1. Theoretical analysis of tensile process

3.1.1. Research background

Based on the multi-scale model of the rock, the change in the position of molecules at the molecular scale during the tensile process is plotted in Fig. 5. When the external load F_L is applied at the boundary of the RVE, the cementing substance between the mineral particles (denoted by the red dotted line in Fig. 5(a)) facilitates tensile deformation. Because the cementing substance is composed of a large number of molecules, the initial position of the molecules is depicted in Fig. 5(b). As the cementing substance facilitates tensile deformation, the distance between the molecules increases; the current position of the molecules is depicted in Fig. 5(c). Once the distance between the molecules becomes equal to r_d, cracks gradually begin to appear. Based on the Lennard-Jones potential and van der Waals force between the non-bonding molecules, the variations in the potential energy and tensile force in the rupture field, from the initial moment of loading to the appearance of cracks, are studied.

Initially, based on the change in the molecular position during the tensile process, two hypotheses are proposed:

(1) The intermolecular distance between the adjacent molecular layers is uniformly distributed from r_{min} to r_{max} at the initial moment of loading, and the increase in the intermolecular distance between the adjacent molecular layers is equal under the external load F_L.

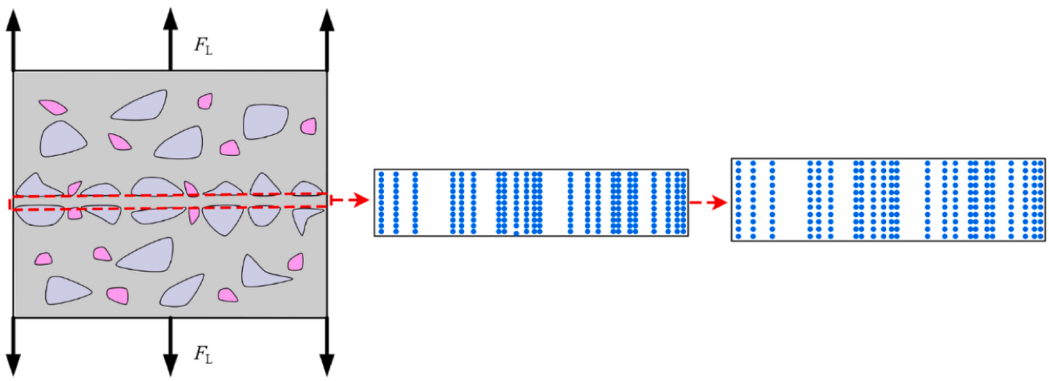

(a) RVE (b) Initial position (c) Current position

Fig. 5. Change in position of molecules at the molecular scale.

(2) The total force between the adjacent molecular layers is equal to the cumulative value of the intermolecular force, which is equal to zero at the initial moment of loading.

3.1.2. Distributed distance

The number of molecules N_f^t at the rupture field boundary (that is, the number of molecules in each molecular layer) in the theoretical model is first determined, and is defined as

$$N_f^t = \frac{S_t \omega}{s_m} \tag{6}$$

where s_m denotes the area occupied by a molecule.

Because the intermolecular distance between the adjacent molecular layers is uniformly distributed from r_{min} to r_{max} at the initial moment of loading and the total force between the adjacent molecular layers is equal to zero, it is expressed as follows:

$$\int_{r_{min}}^{r_{max}} F_{vd}(r) \frac{N_f^t}{r_{max} - r_{min}} dr = 0 \tag{7}$$

Substituting Eq. (2) and Eq. (6) into Eq. (7) finally yields

$$\frac{r_0^{12}}{r_{min}^{12}} - \frac{r_0^6}{r_{min}^6} - \frac{r_0^{12}}{r_{max}^{12}} + \frac{r_0^6}{r_{max}^6} = 0 \tag{8}$$

Assuming $\frac{r_0^6}{r_{min}^6} = A$ and $\frac{r_0^6}{r_{max}^6} = B$, Eq. (8) can be rewritten as

$$A^2 - A - (B^2 - B) = 0 \tag{9}$$

Assuming A^2-$A = B^2$-$B = c$, it can be concluded that A and B are two solutions of x^2-$x = c$:

$$A = \frac{1 + \sqrt{1 + 4c}}{2} \text{ and } B = \frac{1 - \sqrt{1 + 4c}}{2} \tag{10}$$

Therefore, r_{min} and r_{max} are written as

$$r_{min} = \sqrt[6]{\frac{1}{A}} r_0 \text{ and } r_{max} = \sqrt[6]{\frac{1}{B}} r_0 \tag{11}$$

The intermolecular distance between the adjacent molecular layers is in the range of [r_{min}, r_{max}], and increases under the external load F_L. It is assumed that the increase in the distance between any pair of molecules is Δr_v; therefore, the intermolecular distance approximately increases within the range of $r_{min} + \Delta r_v$ to $r_{max} + \Delta r_v$.

3.1.3. Potential energy equation

Because it is assumed that the cementing substance is composed of 11 molecular layers in the theoretical model of the rupture field, the potential energy of the entire rupture field is composed of the potential energy between any two molecular layers. The two molecular layers may be adjacent or separated by 1–4 molecular layers. The potential energy expression between two molecular layers under different conditions is analysed as follows.

For two molecular layers that are adjacent, the intermolecular distance is uniformly distributed in the range of $r_{min} + \Delta r_v$ to $r_{max} + \Delta r_v$, and the potential energy W_{t0} is expressed as

$$\begin{aligned} W_{t0} &= \int_{r_{min}+\triangle r_v}^{r_{max}+\triangle r_v} 4\varepsilon_0 \left(\frac{r_0^{12}}{r^{12}} - \frac{r_0^6}{r^6}\right) \frac{N_f^t}{(r_{max} + \triangle r_v) - (r_{min} + \triangle r_v)} dr \\ &= \frac{4\varepsilon_0 N_f^t}{r_{max} - r_{min}} \int_{r_{min}+\triangle r_v}^{r_{max}+\triangle r_v} \left(\frac{r_0^{12}}{r^{12}} - \frac{r_0^6}{r^6}\right) dr \\ &= \frac{4\varepsilon_0 N_f^t}{r_{max} - r_{min}} \left[\frac{1}{11}\left(\frac{r_0^{12}}{(r_{min} + \triangle r_v)^{11}} - \frac{r_0^{12}}{(r_{max} + \triangle r_v)^{11}}\right) + \frac{1}{5}\left(\frac{r_0^6}{(r_{max} + \triangle r_v)^5} - \frac{r_0^6}{(r_{min} + \triangle r_v)^5}\right)\right] \end{aligned} \tag{12}$$

For two molecular layers that are separated by one molecular layer, the intermolecular distance between the two layers is uniformly distributed in the range of $r_e + r_{min} + 2\Delta r_v$ to $r_e + r_{max} + 2\Delta r_v$, and the potential energy W_{t1} is expressed as

$$W_{t1}=\int_{r_e+r_{min}+2\Delta r_v}^{r_e+r_{max}+2\Delta r_v}4\varepsilon_0\left(\frac{r_0^{12}}{r^{12}}-\frac{r_0^6}{r^6}\right)\frac{N_f^t}{(r_e+r_{max}+2\Delta r_v)-(r_e+r_{min}+2\Delta r_v)}dr$$

$$=\frac{4\varepsilon_0 N_f^t}{r_{max}-r_{min}}\int_{r_e+r_{min}+2\Delta r_v}^{r_e+r_{max}+2\Delta r_v}\left(\frac{r_0^{12}}{r^{12}}-\frac{r_0^6}{r^6}\right)dr \tag{13}$$

$$=\frac{4\varepsilon_0 N_f^t}{r_{max}-r_{min}}\left[\frac{1}{11}\left(\frac{r_0^{12}}{(r_e+r_{min}+2\Delta r_v)^{11}}-\frac{r_0^{12}}{(r_e+r_{max}+2\Delta r_v)^{11}}\right)+\frac{1}{5}\left(\frac{r_0^6}{(r_e+r_{max}+2\Delta r_v)^5}-\frac{r_0^6}{(r_e+r_{min}+2\Delta r_v)^5}\right)\right]$$

For two molecular layers that are separated by two molecular layers in between, the intermolecular distance between these two layers is uniformly distributed in the range of $2r_e + r_{min} + 3\Delta r_v$ to $2r_e + r_{max} + 3\Delta r_v$, and the potential energy W_{t2} is expressed as

$$W_{t2}=\int_{2r_e+r_{min}+3\Delta r_v}^{2r_e+r_{max}+3\Delta r_v}4\varepsilon_0\left(\frac{r_0^{12}}{r^{12}}-\frac{r_0^6}{r^6}\right)\frac{N_f^t}{(2r_e+r_{max}+3\Delta r_v)-(2r_e+r_{max}+3\Delta r_v)}dr$$

$$=\frac{4\varepsilon_0 N_f^t}{r_{max}-r_{min}}\int_{2r_e+r_{min}+3\Delta r_v}^{2r_e+r_{max}+3\Delta r_v}\left(\frac{r_0^{12}}{r^{12}}-\frac{r_0^6}{r^6}\right)dr \tag{14}$$

$$=\frac{4\varepsilon_0 N_f^t}{r_{max}-r_{min}}\left[\frac{1}{11}\left(\frac{r_0^{12}}{(2r_e+r_{min}+3\Delta r_v)^{11}}-\frac{r_0^{12}}{(2r_e+r_{max}+3\Delta r_v)^{11}}\right)+\frac{1}{5}\left(\frac{r_0^6}{(2r_e+r_{max}+3\Delta r_v)^5}-\frac{r_0^6}{(2r_e+r_{min}+3\Delta r_v)^5}\right)\right]$$

Similarly, the potential energy W_{t3} between two molecular layers that are separated by three molecular layers and the potential energy W_{t4} between two molecular layers that are separated by four molecular layers are expressed as follows:

$$W_{t3}=\frac{4\varepsilon_0 N_f^t}{r_{max}-r_{min}}\left[\frac{1}{11}\left(\frac{r_0^{12}}{(3r_e+r_{min}+4\Delta r_v)^{11}}-\frac{r_0^{12}}{(3r_e+r_{max}+4\Delta r_v)^{11}}\right)+\frac{1}{5}\left(\frac{r_0^6}{(3r_e+r_{max}+4\Delta r_v)^5}-\frac{r_0^6}{(3r_e+r_{min}+4\Delta r_v)^5}\right)\right] \tag{15}$$

and

$$W_{t4}=\frac{4\varepsilon_0 N_f^t}{r_{max}-r_{min}}\left[\frac{1}{11}\left(\frac{r_0^{12}}{(4r_e+r_{min}+5\Delta r_v)^{11}}-\frac{r_0^{12}}{(4r_e+r_{max}+5\Delta r_v)^{11}}\right)+\frac{1}{5}\left(\frac{r_0^6}{(4r_e+r_{max}+5\Delta r_v)^5}-\frac{r_0^6}{(4r_e+r_{min}+5\Delta r_v)^5}\right)\right] \tag{16}$$

Based on Eqs. (12)–(16) and the corresponding relation between the actual and theoretical models of the rupture field, the potential energy of the entire rupture field in the actual model is written as

$$\begin{aligned}W_t=\frac{4\varepsilon_0 N_f^t\beta}{r_{max}-r_{min}}\{&10\times\left[\frac{1}{11}\left(\frac{r_0^{12}}{(r_{min}+\triangle r_v)^{11}}-\frac{r_0^{12}}{(r_{max}+\triangle r_v)^{11}}\right)+\frac{1}{5}\left(\frac{r_0^6}{(r_{max}+\triangle r_v)^5}-\frac{r_0^6}{(r_{min}+\triangle r_v)^5}\right)\right]\\&+9\times\left[\frac{1}{11}\left(\frac{r_0^{12}}{(r_e+r_{min}+2\triangle r_v)^{11}}-\frac{r_0^{12}}{(r_e+r_{max}+2\triangle r_v)^{11}}\right)+\frac{1}{5}\left(\frac{r_0^6}{(r_e+r_{max}+2\triangle r_v)^5}-\frac{r_0^6}{(r_e+r_{min}+2\triangle r_v)^5}\right)\right]\\&+8\times\left[\frac{1}{11}\left(\frac{r_0^{12}}{(2r_e+r_{min}+3\triangle r_v)^{11}}-\frac{r_0^{12}}{(2r_e+r_{max}+3\triangle r_v)^{11}}\right)+\frac{1}{5}\left(\frac{r_0^6}{(2r_e+r_{max}+3\triangle r_v)^5}-\frac{r_0^6}{(2r_e+r_{min}+3\triangle r_v)^5}\right)\right]\\&+7\times\left[\frac{1}{11}\left(\frac{r_0^{12}}{(3r_e+r_{min}+4\triangle r_v)^{11}}-\frac{r_0^{12}}{(3r_e+r_{max}+4\triangle r_v)^{11}}\right)+\frac{1}{5}\left(\frac{r_0^6}{(3r_e+r_{max}+4\triangle r_v)^5}-\frac{r_0^6}{(3r_e+r_{min}+4\triangle r_v)^5}\right)\right]\\&+6\times\left[\frac{1}{11}\left(\frac{r_0^{12}}{(4r_e+r_{min}+5\triangle r_v)^{11}}-\frac{r_0^{12}}{(4r_e+r_{max}+5\triangle r_v)^{11}}\right)+\frac{1}{5}\left(\frac{r_0^6}{(4r_e+r_{max}+5\triangle r_v)^5}-\frac{r_0^6}{(4r_e+r_{min}+5\triangle r_v)^5}\right)\right]\}\end{aligned} \tag{17}$$

With the increase in Δr_v, W_t gradually increases, and when Δr_v reaches r_d-r_e, the intermolecular potential energy becomes zero. Therefore, when Δr_v is equal to zero, W_t attains the minimum value, and the absolute value is equal to the tensile fracture energy G_{fl}. This relationship is represented by the following equation:

$$|W_t|\,|_{\triangle r_v=0}=G_{fl} \tag{18}$$

3.1.4. Equation of force

Based on the characteristics of the Lennard-Jones potential and van der Waals force, it can be concluded that the outermost molecular layer of the rupture field in the theoretical model bears the intermolecular force from other layers. These two molecular layers may be adjacent or separated by 1–4 molecular layers. The force equation between two molecular layers under different conditions is analysed as follows.

For two molecular layers that are adjacent, the intermolecular distance is uniformly distributed from $r_{min} + \Delta r_v$ to $r_{max} + \Delta r_v$, and the force F_{t0} is expressed as

$$F_{t0}=\int_{r_{min}+\Delta r_v}^{r_{max}+\Delta r_v}\frac{24\varepsilon_0}{r_0}\left(\frac{2r_0^{13}}{r^{13}}-\frac{r_0^7}{r^7}\right)\frac{N_f^t}{(r_{max}+\Delta r_v)-(r_{min}+\Delta r_v)}\mathrm{d}r$$
$$=\frac{24\varepsilon_0}{r_0}\frac{N_f^t}{r_{max}-r_{min}}\int_{r_{min}+\Delta r_v}^{r_{max}+\Delta r_v}\left(\frac{2r_0^{13}}{r^{13}}-\frac{r_0^7}{r^7}\right)\mathrm{d}r \tag{19}$$
$$=\frac{4\varepsilon_0 N_f^t}{r_{max}-r_{min}}\left[\left(\frac{-r_0^{12}}{(r_{max}+\Delta r_v)^{12}}+\frac{r_0^{12}}{(r_{min}+\Delta r_v)^{12}}\right)-\left(\frac{-r_0^6}{(r_{max}+\Delta r_v)^6}+\frac{r_0^6}{(r_{min}+\Delta r_v)^6}\right)\right]$$

For two molecular layers that are separated by one molecular layer, the intermolecular distance between the two layers is uniformly distributed from $r_e + r_{min} + 2\Delta r_v$ to $r_e + r_{max} + 2\Delta r_v$, and the force F_{t1} is expressed as

$$F_{t1}=\int_{r_e+r_{min}+2\Delta r_v}^{r_e+r_{max}+2\Delta r_v}\frac{24\varepsilon_0}{r_0}\left(\frac{2r_0^{13}}{r^{13}}-\frac{r_0^7}{r^7}\right)\frac{N_f^t}{(r_e+r_{max}+2\Delta r_v)-(r_e+r_{min}+2\Delta r_v)}\mathrm{d}r$$
$$=\frac{24\varepsilon_0}{r_0}\frac{N_f^t}{r_{max}-r_{min}}\int_{r_e+r_{min}+2\Delta r_v}^{r_e+r_{max}+2\Delta r_v}\left(\frac{2r_0^{13}}{r^{13}}-\frac{r_0^7}{r^7}\right)\mathrm{d}r \tag{20}$$
$$=\frac{4\varepsilon_0 N_f^t}{r_{max}-r_{min}}\left[\left(\frac{-r_0^{12}}{(r_e+r_{max}+2\Delta r_v)^{12}}+\frac{r_0^{12}}{(r_e+r_{min}+2\Delta r_v)^{12}}\right)-\left(\frac{-r_0^6}{(r_e+r_{max}+2\Delta r_v)^6}+\frac{r_0^6}{(r_e+r_{min}+2\Delta r_v)^6}\right)\right]$$

For two molecular layers that are separated by two molecular layers in between, the intermolecular distance between the two layers is uniformly distributed from $2r_e + r_{min} + 3\Delta r_v$ to $2r_e + r_{max} + 3\Delta r_v$, and the force F_{t2} is expressed as

$$F_{t2}=\int_{2r_e+r_{min}+3\Delta r_v}^{2r_e+r_{max}+3\Delta r_v}\frac{24\varepsilon_0}{r_0}\left(\frac{2r_0^{13}}{r^{13}}-\frac{r_0^7}{r^7}\right)\frac{N_f^t}{(2r_e+r_{max}+3\Delta r_v)-(2r_e+r_{min}+3\Delta r_v)}\mathrm{d}r$$
$$=\frac{24\varepsilon_0}{r_0}\frac{N_f^t}{r_{max}-r_{min}}\int_{2r_e+r_{min}+3\Delta r_v}^{2r_e+r_{max}+3\Delta r_v}\left(\frac{2r_0^{13}}{r^{13}}-\frac{r_0^7}{r^7}\right)\mathrm{d}r \tag{21}$$
$$=\frac{4\varepsilon_0 N_f^t}{r_{max}-r_{min}}\left[\left(\frac{-r_0^{12}}{(2r_e+r_{max}+3\Delta r_v)^{12}}+\frac{r_0^{12}}{(2r_e+r_{min}+3\Delta r_v)^{12}}\right)-\left(\frac{-r_0^6}{(2r_e+r_{max}+3\Delta r_v)^6}+\frac{r_0^6}{(2r_e+r_{min}+3\Delta r_v)^6}\right)\right]$$

Similarly, the force F_{t3} between two molecular layers that are separated by three molecular layers and the force F_{t4} between two molecular layers that are separated by four molecular layers are expressed as

$$F_{t3}=\frac{4\varepsilon_0 N_f^t}{r_{max}-r_{min}}\left[\left(\frac{-r_0^{12}}{(3r_e+r_{max}+4\Delta r_v)^{12}}+\frac{r_0^{12}}{(3r_e+r_{min}+4\Delta r_v)^{12}}\right)-\left(\frac{-r_0^6}{(3r_e+r_{max}+4\Delta r_v)^6}+\frac{r_0^6}{(3r_e+r_{min}+4\Delta r_v)^6}\right)\right] \tag{22}$$

and

$$F_{t4}=\frac{4\varepsilon_0 N_f^t}{r_{max}-r_{min}}\left[\left(\frac{-r_0^{12}}{(4r_e+r_{max}+5\Delta r_v)^{12}}+\frac{r_0^{12}}{(4r_e+r_{min}+5\Delta r_v)^{12}}\right)-\left(\frac{-r_0^6}{(4r_e+r_{max}+5\Delta r_v)^6}+\frac{r_0^6}{(4r_e+r_{min}+5\Delta r_v)^6}\right)\right] \tag{23}$$

Based on Eqs. (19)–(23) and the corresponding relation between the actual and theoretical models of the rupture field, the force of the entire rupture field in the actual model is expressed as

$$\begin{aligned}F_t=\frac{4\varepsilon_0 N_f^t}{r_{max}-r_{min}}\{&\left[\left(\frac{-r_0^{12}}{(r_{max}+\Delta r_v)^{12}}+\frac{r_0^{12}}{(r_{min}+\Delta r_v)^{12}}\right)-\left(\frac{-r_0^6}{(r_{max}+\Delta r_v)^6}+\frac{r_0^6}{(r_{min}+\Delta r_v)^6}\right)\right]\\&+\left[\left(\frac{-r_0^{12}}{(r_e+r_{max}+2\Delta r_v)^{12}}+\frac{r_0^{12}}{(r_e+r_{min}+2\Delta r_v)^{12}}\right)-\left(\frac{-r_0^6}{(r_e+r_{max}+2\Delta r_v)^6}+\frac{r_0^6}{(r_e+r_{min}+2\Delta r_v)^6}\right)\right]\\&+\left[\left(\frac{-r_0^{12}}{(2r_e+r_{max}+3\Delta r_v)^{12}}+\frac{r_0^{12}}{(2r_e+r_{min}+3\Delta r_v)^{12}}\right)-\left(\frac{-r_0^6}{(2r_e+r_{max}+3\Delta r_v)^6}+\frac{r_0^6}{(2r_e+r_{min}+3\Delta r_v)^6}\right)\right]\\&+\left[\left(\frac{-r_0^{12}}{(3r_e+r_{max}+4\Delta r_v)^{12}}+\frac{r_0^{12}}{(3r_e+r_{min}+4\Delta r_v)^{12}}\right)-\left(\frac{-r_0^6}{(3r_e+r_{max}+4\Delta r_v)^6}+\frac{r_0^6}{(3r_e+r_{min}+4\Delta r_v)^6}\right)\right]\\&+\left[\left(\frac{-r_0^{12}}{(4r_e+r_{max}+5\Delta r_v)^{12}}+\frac{r_0^{12}}{(4r_e+r_{min}+5\Delta r_v)^{12}}\right)-\left(\frac{-r_0^6}{(4r_e+r_{max}+5\Delta r_v)^6}+\frac{r_0^6}{(4r_e+r_{min}+5\Delta r_v)^6}\right)\right]\}\end{aligned} \tag{24}$$

F_t is negative and positive for tensile force and compressive force, respectively. When Δr_v gradually increases from zero, the absolute value of F_t increases initially and subsequently decreases. When $\Delta r_v = r_s\text{-}r_e$, the absolute value of F_t attains the maximum value, and it is equal to the value of the tensile strength σ_t. Therefore, F_t is expressed as

$$|F_t|\,|_{\triangle r_v=r_s-r_e}=\sigma_t \tag{25}$$

3.2. Theoretical analysis of shear

3.2.1. Research background

Based on the multi-scale model of the rock, the change in the position of molecules at the molecular scale during the shear process is plotted in Fig. 6. When the external load F_L is applied at the boundary of the RVE, the cementing substance between the mineral particles (denoted by the red dotted line in Fig. 6(a)) facilitates shear deformation. The cementing substance is composed of a large number of molecules, and the initial position of the molecules is depicted in Fig. 6(b). As the cementing substance facilitates shear deformation, the tangential distance between the molecules increases; the current position of the molecules is depicted in Fig. 6(c). Once the distance between the molecules reaches r_d, cracks gradually begin to appear. Based on the Lennard-Jones potential and van der Waals force, the changes in the potential energy and shear force in the rupture field from the initial moment of loading to the appearance of cracks, are studied.

Based on the change in the molecular position during the shear process, two hypotheses are proposed:

(1) During the shear process, the tangential increase in the intermolecular distance between the adjacent molecular layers is equal under the external load F_L.
(2) The total force between the adjacent molecular layers is equal to the cumulative value of the intermolecular force, which is equal to zero at the initial moment of loading.

3.2.2. Distributed distance

For two adjacent molecular layers at the molecular scale, new intermolecular forces may be experienced by the molecules that originally did not possess intermolecular forces because of the tangential change in the spatial position during the shear process. Therefore, the contact ratio λ is proposed to quantify the increase in the number of molecules possessing the intermolecular force during the shear process. Based on the number of molecules at the rupture field boundary and contact ratio λ, the number of molecules N_f^s possessing intermolecular force between the adjacent molecular layers during the shear process is defined as

$$N_f^s = \frac{S_t \omega \lambda}{s_m} \tag{26}$$

It is assumed that the intermolecular distance between the adjacent molecular layers is uniformly distributed from r_{min} to r_{max} at the initial moment of loading in Section 3.1.2. However, to simplify the force and potential energy equations during the shear process, it is assumed that the intermolecular distance between the adjacent molecular layers is equal to r_e at the initial moment of loading. Under this distribution condition, the total force between the adjacent molecular layers is still zero, which is consistent with the value when the intermolecular distance is uniformly distributed from r_{min} to r_{max}. However, once the intermolecular distance becomes equal to r_e, the potential energy between the adjacent molecular layers becomes greater than that under the uniform distribution of r_{min}–r_{max}. Therefore, a dimensionless coefficient η is proposed, and is defined as

$$\eta = \frac{w_{lj}(r_e) N_f^s}{\int_{r_{min}}^{r_{max}} w_{lj}(r) \frac{N_f^s}{r_{max}-r_{min}} dr} \approx 1.2566 \tag{27}$$

When the expressions of the potential energy and force are obtained under the condition wherein the intermolecular distance is r_e, the potential energy and force should be divided by η.

The change in the spatial position of two molecules in adjacent molecular layers during the shear process is plotted in Fig. 7. Fig. 7 (a) illustrates the initial position of two molecules, and it can be observed that the vertical position difference is r_e and the tangential position difference is zero. When shear deformation occurs, the current position of the two molecules is plotted in Fig. 7(b). It can be observed that the vertical position difference is still r_e, and the tangential position difference is Δr_u. The distance r between molecule A′ and molecule B′ is equal to $\sqrt{r_e^2 + (\triangle r_u)^2}$.

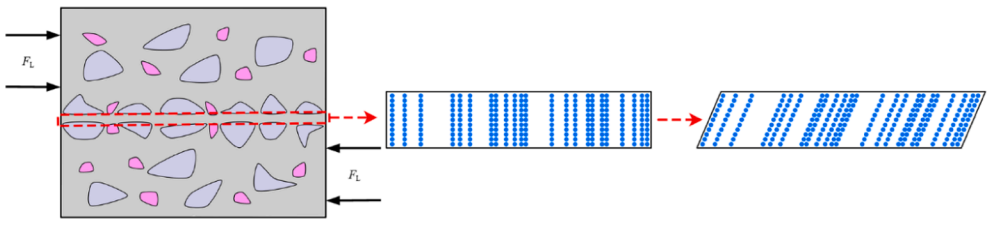

(a) RVE (b) Initial position (c) Current position

Fig. 6. Change in the position of molecules at the molecular scale.

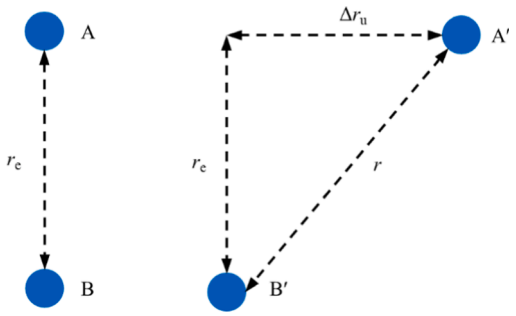

(a) Initial position (b) Current position

Fig. 7. Change in the spatial position of two molecules during the shear process.

3.2.3. Potential energy expression

Because it is assumed that the cementing substance is composed of 11 molecular layers in the theoretical model of the rupture field, the potential energy of the entire rupture field is composed of the potential energy between any two molecular layers. The two molecular layers may be adjacent or separated by 1–4 molecular layers. The potential energy relationship between two molecular layers under different conditions is analysed as follows.

For two molecular layers that are adjacent, the vertical intermolecular distance is r_e, and the potential energy W_{s0} is expressed as

$$W_{s0} = \frac{4\varepsilon_0 N_f^s}{1.2566}\left[\left(\frac{r_0}{\sqrt{r_e^2 + (\triangle r_u)^2}}\right)^{12} - \left(\frac{r_0}{\sqrt{r_e^2 + (\triangle r_u)^2}}\right)^{6}\right] \tag{28}$$

For two molecular layers that are separated by one molecular layer, the vertical intermolecular distance is $2r_e$, and the potential energy W_{s1} is expressed as

$$W_{s1} = \frac{4\varepsilon_0 N_f^s}{1.2566}\left[\left(\frac{r_0}{\sqrt{(2r_e)^2 + (2\triangle r_u)^2}}\right)^{12} - \left(\frac{r_0}{\sqrt{(2r_e)^2 + (2\triangle r_u)^2}}\right)^{6}\right] \tag{29}$$

For two molecular layers that are separated by two molecular layers, the vertical intermolecular distance is $3r_e$, and the potential energy W_{s2} is expressed as

$$W_{s2} = \frac{4\varepsilon_0 N_f^s}{1.2566}\left[\left(\frac{r_0}{\sqrt{(3r_e)^2 + (3\triangle r_u)^2}}\right)^{12} - \left(\frac{r_0}{\sqrt{(3r_e)^2 + (3\triangle r_u)^2}}\right)^{6}\right] \tag{30}$$

Similarly, the potential energy W_{s3} between two molecular layers that are separated by three molecular layers and the potential energy W_{s4} between two molecular layers that are separated by four molecular layers are expressed as

$$W_{s3} = \frac{4\varepsilon_0 N_f^s}{1.2566}\left[\left(\frac{r_0}{\sqrt{(4r_e)^2 + (4\triangle r_u)^2}}\right)^{12} - \left(\frac{r_0}{\sqrt{(4r_e)^2 + (4\triangle r_u)^2}}\right)^{6}\right] \tag{31}$$

and

$$W_{s4} = \frac{4\varepsilon_0 N_f^s}{1.2566}\left[\left(\frac{r_0}{\sqrt{(5r_e)^2 + (5\triangle r_u)^2}}\right)^{12} - \left(\frac{r_0}{\sqrt{(5r_e)^2 + (5\triangle r_u)^2}}\right)^{6}\right] \tag{32}$$

Based on Eqs. (28)–(32) and the corresponding relationship between the actual and theoretical models of the rupture field, the potential energy of the entire rupture field in the actual model is expressed as

$$\begin{aligned} W_s = \frac{4\varepsilon_0 N_f^s \beta}{1.2566}\{&10\times\left[\left(\frac{r_0}{\sqrt{r_e^2 + (\triangle r_u)^2}}\right)^{12} - \left(\frac{r_0}{\sqrt{r_e^2 + (\triangle r_u)^2}}\right)^{6}\right] \\ &+9\times\left[\left(\frac{r_0}{\sqrt{(2r_e)^2 + (2\triangle r_u)^2}}\right)^{12} - \left(\frac{r_0}{\sqrt{(2r_e)^2 + (2\triangle r_u)^2}}\right)^{6}\right] + 8\times\left[\left(\frac{r_0}{\sqrt{(3r_e)^2 + (3\triangle r_u)^2}}\right)^{12} - \left(\frac{r_0}{\sqrt{(3r_e)^2 + (3\triangle r_u)^2}}\right)^{6}\right] \\ &+7\times\left[\left(\frac{r_0}{\sqrt{(4r_e)^2 + (4\triangle r_u)^2}}\right)^{12} - \left(\frac{r_0}{\sqrt{(4r_e)^2 + (4\triangle r_u)^2}}\right)^{6}\right] + 6\times\left[\left(\frac{r_0}{\sqrt{(5r_e)^2 + (5\triangle r_u)^2}}\right)^{12} - \left(\frac{r_0}{\sqrt{(5r_e)^2 + (5\triangle r_u)^2}}\right)^{6}\right]\} \end{aligned} \tag{33}$$

When Δr_u is equal to zero, W_s attains the minimum value, and the absolute value is equal to the shear fracture energy G_{fII}. This relationship is expressed as

$$|W_s|\,|_{\triangle r_u = 0} = G_{fII} \tag{34}$$

3.2.4. Equation of force

Based on the characteristics of the Lennard-Jones potential and van der Waals force, it can be concluded that the outermost molecular layer in the theoretical model bears the intermolecular force from the other layers. These two molecular layers may be adjacent or separated by 1–4 molecular layers. The force relationship between two molecular layers under different conditions is analysed.

For two molecular layers that are adjacent, the vertical intermolecular distance is r_e, and the force F_{s0} is expressed as

$$F_{s0} = \frac{24\varepsilon_0 \triangle r_u N_f^s}{1.2566 r_0 r}\left[\frac{2r_0^{13}}{(r_e^2 + (\triangle r_u)^2)^{\frac{13}{2}}} - \frac{r_0^7}{(r_e^2 + (\triangle r_u)^2)^{\frac{7}{2}}}\right] \tag{35}$$

For two molecular layers that are separated by one molecular layer, the vertical intermolecular distance is $2r_e$, and the force F_{s1} is expressed as

$$F_{s1} = \frac{24\varepsilon_0 \triangle r_u N_f^s}{1.2566 r_0 r}\left[\frac{2r_0^{13}}{((2r_e)^2 + (2\triangle r_u)^2)^{\frac{13}{2}}} - \frac{r_0^7}{((2r_e)^2 + (2\triangle r_u)^2)^{\frac{7}{2}}}\right] \tag{36}$$

For two molecular layers that are separated by two molecular layers, the vertical intermolecular distance is $3r_e$, and the force F_{s2} is expressed as

$$F_{s2} = \frac{24\varepsilon_0 \triangle r_u N_f^s}{1.2566 r_0 r}\left[\frac{2r_0^{13}}{((3r_e)^2 + (3\triangle r_u)^2)^{\frac{13}{2}}} - \frac{r_0^7}{((3r_e)^2 + (3\triangle r_u)^2)^{\frac{7}{2}}}\right] \tag{37}$$

Similarly, the force F_{s3} between two molecular layers that are separated by three molecular layers and the force F_{s4} between two molecular layers that are separated by four molecular layers are expressed as

$$F_{s3} = \frac{24\varepsilon_0 \triangle r_u N_f^s}{1.2566 r_0 r}\left[\frac{2r_0^{13}}{((4r_e)^2 + (4\triangle r_u)^2)^{\frac{13}{2}}} - \frac{r_0^7}{((4r_e)^2 + (4\triangle r_u)^2)^{\frac{7}{2}}}\right] \tag{38}$$

and

$$F_{s4} = \frac{24\varepsilon_0 \triangle r_u N_f^s}{1.2566 r_0 r}\left[\frac{2r_0^{13}}{((5r_e)^2 + (5\triangle r_u)^2)^{\frac{13}{2}}} - \frac{r_0^7}{((5r_e)^2 + (5\triangle r_u)^2)^{\frac{7}{2}}}\right] \tag{39}$$

Based on Eqs. (35)–(39) and the corresponding relation between the actual and theoretical models of the rupture field, the shear force of the entire rupture field in the actual model is expressed as

$$\begin{aligned} F_s = \frac{24\varepsilon_0 \triangle r_u N_f^s}{1.2566 r_0 r}\{&\left[\frac{2r_0^{13}}{(r_e^2 + (\triangle r_u)^2)^{\frac{13}{2}}} - \frac{r_0^7}{(r_e^2 + (\triangle r_u)^2)^{\frac{7}{2}}}\right] \\ &+\left[\frac{2r_0^{13}}{((2r_e)^2 + (2\triangle r_u)^2)^{\frac{13}{2}}} - \frac{r_0^7}{((2r_e)^2 + (2\triangle r_u)^2)^{\frac{7}{2}}}\right] + \left[\frac{2r_0^{13}}{((3r_e)^2 + (3\triangle r_u)^2)^{\frac{13}{2}}} - \frac{r_0^7}{((3r_e)^2 + (3\triangle r_u)^2)^{\frac{7}{2}}}\right] \\ &+\left[\frac{2r_0^{13}}{((4r_e)^2 + (4\triangle r_u)^2)^{\frac{13}{2}}} - \frac{r_0^7}{((4r_e)^2 + (4\triangle r_u)^2)^{\frac{7}{2}}}\right] + \left[\frac{2r_0^{13}}{((5r_e)^2 + (5\triangle r_u)^2)^{\frac{13}{2}}} - \frac{r_0^7}{((5r_e)^2 + (5\triangle r_u)^2)^{\frac{7}{2}}}\right]\} \end{aligned} \tag{40}$$

Based on the multi-scale model of the rock and Lennard-Jones potential, the force and potential energy equations in the novel cohesive fracture model during the tensile and shear processes are obtained.

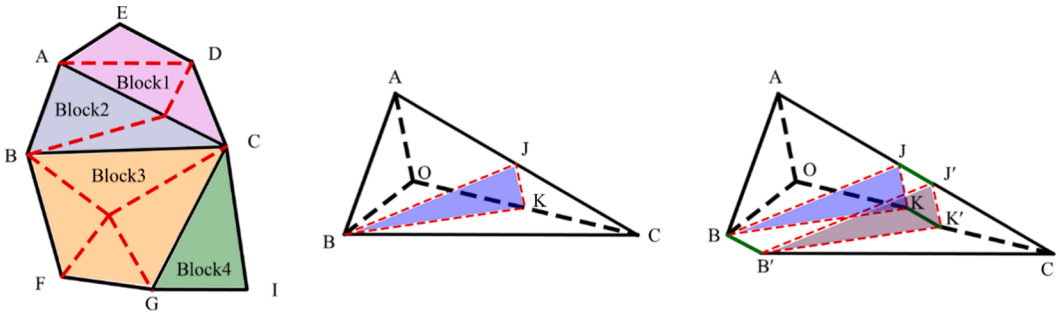

(a) Blocks and interfaces (b) Virtual interface (c) Numerical springs

Fig. 8. Schematic of blocks and interfaces.

4. Numerical results

To study the accuracy of the novel cohesive fracture model in simulating the rock fracture process, numerical simulations are conducted for three cases by introducing the novel cohesive fracture model into the continuum-discontinuum element method (CDEM).

4.1. Basic concept of CDEM

4.1.1. Numerical model of CDEM

The continuum-discontinuum element method (CDEM) is a dynamic explicit algorithm, and it can simulate the entire process from continuous deformation to crack formation and propagation [67,68]. The numerical model of CDEM is composed of blocks and interfaces (as shown in Fig. 8). A block includes one or more elements, and it is used to characterise the continuous features of the material. The common boundary between the blocks is defined as the interface that is used to characterise the discontinuous features. The interface includes the real interface (denoted by the black solid lines in Fig. 8(a)) and the virtual interface (denoted by the red dotted lines in Fig. 8(a)). The real interface represents the real discontinuous features of the material. The virtual interface has two main functionalities: to connect blocks and transfer mechanical information and to provide the potential space for crack initiation and propagation. To accurately calculate the contact force and failure state between the blocks, a semi-spring and semi-edge combined contact model is introduced by the CDEM at the interface (the green line BB′, JJ′, and KK′ in Fig. 8(c)) [69]. Because the mechanical behaviour of the interface is realised by numerical springs, the cohesive fracture model is adopted as the constitutive model of numerical springs at the interface.

The governing equation of CDEM is established through the Langrage energy system, and the governing equation can finally be written as

$$\boldsymbol{M}\ddot{\boldsymbol{u}}(t) + \boldsymbol{C}\dot{\boldsymbol{u}}(t) + \boldsymbol{K}\boldsymbol{u}(t) = \boldsymbol{F}(t) \tag{41}$$

where $\ddot{\boldsymbol{u}}(t)$, $\dot{\boldsymbol{u}}(t)$, and $\boldsymbol{u}(t)$ denote the acceleration vector, velocity vector, and displacement vector, respectively. $\boldsymbol{M}$, $\boldsymbol{C}$, and $\boldsymbol{K}$ denote the mass, damping, and stiffness matrices, respectively. $\boldsymbol{F}(t)$ is the vector of the external force.

Solving the governing Eq. (41) is the most important aspect of the CDEM calculation, which uses the explicit Eulerian precession method based on an incremental method to solve the problem. For the iterative solution in each time-step, the calculation is divided into two parts: the first step is to loop each element to calculate the continuous deformation; the second step is to calculate the force at the interface.

4.1.2. Constitutive model of element

In the numerical model of CDEM, the block is used to characterise the continuous features of the material, and includes one or more elements. CDEM provides many constitutive models for elements, including the linear elastic constitutive model, Mohr-Coulomb elastoplastic constitutive model, and Drucker-Prager elastoplastic constitutive model. In this study, the linear elastic constitutive model is adopted as the constitutive model of the element, which can simulate the elastic deformation of the material.

In the linear elastic constitutive model, the element stress increment $\Delta\sigma_{ij}$ at time-step t is first calculated using the incremental form of the finite element method; the corresponding equation is as follows:

$$\Delta\sigma_{ij} = 2G\Delta\varepsilon_{ij} + (K - \frac{2}{3}G)\Delta\theta\delta_{ij} \tag{42}$$

where $\Delta\sigma_{ij}$ is the element stress increment at time-step t, $\Delta\varepsilon_{ij}$ is the element strain increment at time-step t, $\Delta\theta$ is the element bulk strain increment at time-step t, K is the bulk modulus, G is the shear modulus, and δ_{ij} is the Kronecker symbol.

Subsequently, the trial stress of the element at time-step t is calculated using the following equation:

$$\sigma_{ij} = \Delta\sigma_{ij} + \sigma_{ij\text{ - old}} \tag{43}$$

where σ_{ij} is the element trial stress at time-step t, and $\sigma_{ij\text{-old}}$ is the element stress at the last time-step.

In the linear elastic constitutive model, σ_{ij} is considered as the real stress of the element for the mechanical calculation. In other constitutive models, such as the Mohr-Coulomb elastoplastic constitutive model, element trial stress σ_{ij} will be analyzed. If σ_{ij} satisfies the Mohr-Coulomb criterion, it will be modified. If not, it will be directly adopted as the real stress of the element to participate in the mechanical calculation.

4.1.3. Constitutive model of interface

In Section 3, a new cohesive fracture model based on the multi-scale model and Lennard-Jones potential is proposed, and is adopted as the constitutive model of interfaces. In the numerical calculation of interfaces, the nodal space position of the elements on both sides of the interface is first obtained; subsequently, the deformation of the interface is calculated. It may be noted that the deformation of the interface is reflected at the particle scale. Thereafter, based on the corresponding relation of deformation at the particle scale and molecular scale, the change in the intermolecular distance at the molecular scale is calculated. Finally, the force applied to the elements by numerical springs is obtained; the energy of the elements and interface changes during this process. Once the interface breaks, the change in the potential energy of the interface is equal to the value of the fracture energy.

To reduce the computational complexity, the equation of force (Eq. (24) and Eq. (40)) are simplified. The equation of force during the tensile process is written as Eq. (44), and the equation of force during the shear process is written as Eq. (45). As the intermolecular displacement increases, the changing curves of the force are plotted in Fig. 9, and the area under the changing curves denotes the tensile fracture energy G_{fI} (Fig. 9(a)) and shear fracture energy G_{fII} (Fig. 9(b)).

To obtain the value of the force applied to the elements by numerical springs based on Eq. (44) and Eq. (45), the value of the key parameters (thickness ratio β, space occupancy ratio ω and contact ratio λ) should be calculated first. Therefore, the tensile strength σ_{t}, tensile fracture energy G_{fI} and shear fracture energy G_{fII} should be obtained first, and the value of β, ω and λ are calculated based on Eq. (18), Eq. (25) and Eq. (34).

$$F_{\mathrm{t}} \approx \frac{4.1304\varepsilon_0 N_{\mathrm{f}}^{\mathrm{t}}}{r_{max}-r_{min}}\left[\left(\frac{-r_0^{12}}{(\Delta r_{\mathrm{v}}+r_{max})^{12}}+\frac{r_0^{12}}{(\Delta r_{\mathrm{v}}+r_{min})^{12}}\right)-\left(\frac{-r_0^{6}}{(\Delta r_{\mathrm{v}}+r_{max})^{6}}+\frac{r_0^{6}}{(\Delta r_{\mathrm{v}}+r_{min})^{6}}\right)\right] \tag{44}$$

$$F_{\mathrm{s}} \approx \frac{19.7218\varepsilon_0 \triangle r_{\mathrm{u}} N_{\mathrm{f}}^{\mathrm{s}}}{r_0 r_{\mathrm{e}}}\left[\frac{2r_0^{13}}{(r_{\mathrm{e}}^2+(\triangle r_{\mathrm{u}})^2)^{\frac{13}{2}}}-\frac{r_0^{7}}{(r_{\mathrm{e}}^2+(\triangle r_{\mathrm{u}})^2)^{\frac{7}{2}}}\right] \tag{45}$$

4.2. Numerical cases

To study the accuracy of the cohesive fracture model in simulating the fracture process of rocks, numerical simulations corresponding to three cases (that is, Mode-I test, Mode-II test and uniaxial compression test) are conducted.

4.2.1. Mode-I test

The numerical simulation of Mode-I test mainly studies whether the cohesive fracture model can accurately characterise the tensile strength and tensile fracture energy of rocks during the tensile process. The Mode-I test is conducted on a rectangular model with a dimension of 10 cm × 20 cm, and the numerical model is plotted in Fig. 10. It can be observed that there is a virtual interface (the dotted line in Fig. 10) in the middle of the numerical model. The linear elastic model is adopted as the constitutive model of the element, and the cohesive fracture model is adopted as the constitutive model of the virtual interface. A tensile velocity is applied at the top and bottom boundaries of the numerical model, and the velocity is $v_{\mathrm{y}} = 1 \times 10^{-8}$ m/s. In the CDEM-based simulation of the Mode-I test, the mechanical parameters that need to be input include the mechanical parameters of the element as well as the interface. Because the constitutive model of element is the linear elastic model, the density, Young's modulus and Poisson's ratio must be provided as inputs to the model. For the interface, the tensile strength, tensile fracture energy and shear fracture energy must be provided as inputs to calculate the value of the thickness ratio β, space occupancy ratio ω and contact ratio λ. The mechanical parameters are shown in Table 1, and the parameters in the table are the generalised values of rocks.

The displacement-force curves of the top and bottom boundaries are plotted in Fig. 11; the x-axis represents the displacement of the boundary, and the y-axis represents the force of the boundary. The curves evidently exhibit a three-stage characteristic. In the OA range, the force increases rapidly with the increase in the displacement. In the AB range, the force decreases rapidly with the increase in the displacement. In the BC range, the force is close to zero, and finally it reduces to zero with the increase in the displacement. Once the intermolecular distance reaches r_{d}, tensile failure occurs at the interface, and the force becomes zero. Based on the numerical result, it is concluded that the tensile force at point A is 102.0 kN, and the corresponding tensile stress is 1.02 MPa. Compared with the tensile strength $\sigma_{\mathrm{t}} = 1$ MPa in Table 1, the error is 2.0%. Therefore, it is determined that the cohesive fracture model can accurately characterise the tensile strength of rocks during the tensile process.

To quantify the degree of crack and obtain the changing trend of the cracks, a dimensionless index, crack ratio α, is introduced, and it is expressed as

$$\alpha = \frac{S_{\mathrm{c}}}{S_{\mathrm{e}}} \tag{46}$$

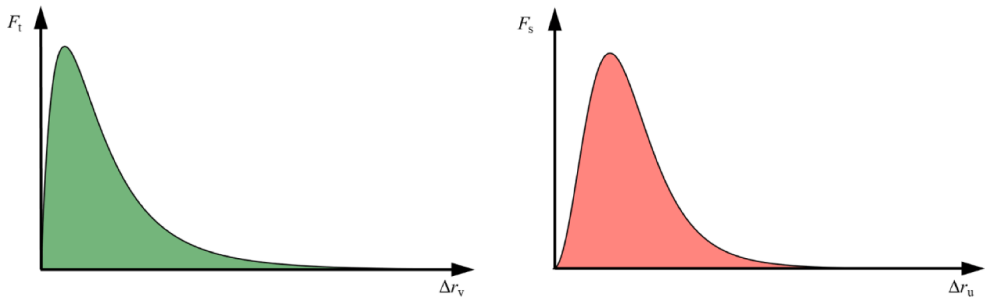

(a) Tensile process (b) Shear process

Fig. 9. Intermolecular displacement-force curves.

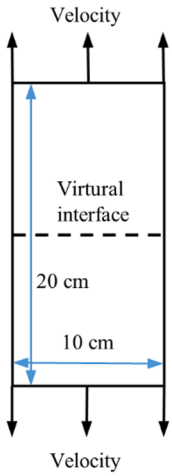

Fig. 10. Numerical model of Mode-I test.

Table 1
Mechanical parameters in Mode-I test.

Density (kg/m^3)	Young's modulus (GPa)	Poisson's ratio	Tensile strength (MPa)	Tensile fracture energy (J/m^2)	Shear fracture energy (J/m^2)
2500	10	0.25	1	100	1000

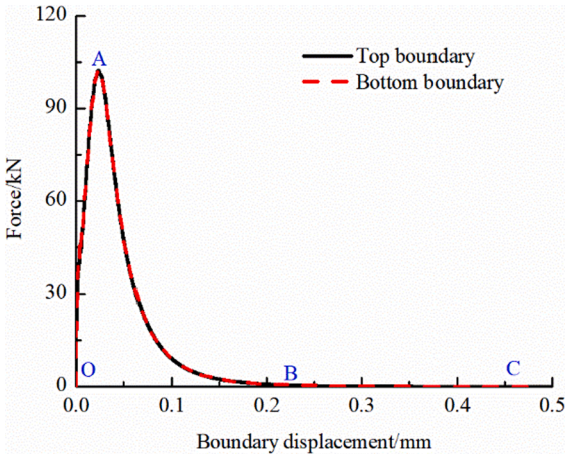

Fig. 11. Displacement-force curves.

where S_c denotes the area of the cracked interface, and S_e denotes the area of the entire interface. It can be observed that the value range of α is [0, 1].

The curve corresponding to the change in the crack ratio α during the tensile process is plotted in Fig. 12; x-axis represents the displacement of the boundary, and y-axis represents the crack ratio α. The curve evidently exhibits a three-stage characteristic, as can be observed in Fig. 12(a). In the OD range, the crack ratio α does not change with the increase in the displacement. In the DE range, the crack ratio α increase sharply from 0 to 1 with the increase in the displacement. In the EC range, the crack ratio does not change, and it is always 1.

Based on Fig. 11 and Fig. 12(a), it can be seen that when the boundary displacement reaches point B, the boundary force is close to zero; however, the interface is still not broken at the moment. As the boundary displacement increases, the interface begins to break when the boundary displacement increases to point D. Once the boundary displacement increases to point E, the entire interface breaks, and the boundary force reduces to zero.

To more accurately obtain the changing trend of the crack ratio α, the boundary displacement-crack ratio curve in the DE range is plotted in Fig. 12(b). It can be observed that the crack ratio α increases linearly from 0 to 1 with the increase in the displacement in the DE range.

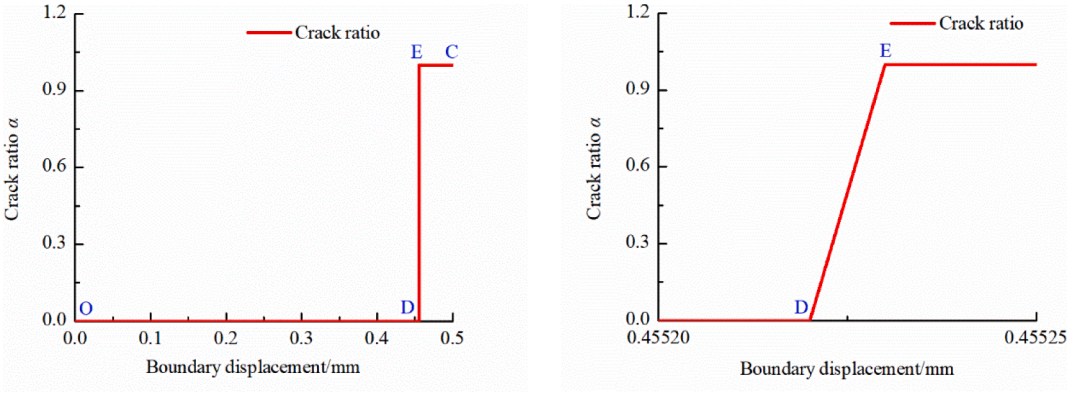

(a) Whole curve (b) Local curve in DE range

Fig. 12. Boundary displacement-crack ratio α curve.

Fig. 13 plots the intermolecular displacement-force curve corresponding to ID = 50 for the numerical spring (in the middle of the interface). It can be observed that the curve exhibits a three-stage characteristic, and the area under the changing curves denotes the tensile fracture energy. To obtain the tensile fracture energy, the value of the area under the curve is first obtained by integration which represents only the value of the tensile fracture energy at the molecular scale. Subsequently, the tensile fracture energy at the particle scale is obtained based on the corresponding relation of the deformation at the molecular scale and particle scale; the numerical value of the spring tensile fracture energy is calculated to be 0.05 J. Because the area represented by the numerical spring is 5×10^{-4} m^2, it is concluded that the theoretical value of the spring tensile fracture energy is 0.05 J under the premise that the tensile fracture energy G_{fl} = 100 J/m^2. It can be concluded that the numerical value and theoretical value of the tensile fracture energy are equal. In addition, the peak tensile strength corresponding to point A is 1.01 MPa, and the error is 1%, compared with the theoretical value of 1 MPa.

To further evaluate the novel cohesive fracture model, the experimental results of the semi-circular bend are used for comparison. Wei et al. [70] conducted the laboratory experiment of sandstone, quarried from Dazhou, Sichuan province of China. The schematic of the SCB numerical model is shown in Fig. 14, and Table 2 lists the details of the basic notations. The tensile strength is 4.6 MPa, the Young's modulus is 16.5 GPa and the Poisson's ratio is 0.22. The linear elastic model is adopted as the constitutive model of the element, and the cohesive fracture model is adopted as the constitutive model of the interface. A vertical velocity $v_y = 2 \times 10^{-8}$ m/s is applied at the top boundary, and the bottom boundary is sustained by two supporting rolls.

A comparison of the numerical and experimental load point displacement-force curves in the SCB test is plotted in Fig. 15. It can be observed that the changing trends of the curves are similar. Before the load point displacement reaches the peak value, with the increase in the displacement, the force gradually increases. Once the displacement reaches the peak value, the force decreases rapidly. The values of the peak displacement and peak force in the laboratory test and numerical simulation are similar. In the laboratory test, when the displacement reaches 0.25 mm, the force reaches the maximum value of 1176 N. In the numerical simulation, when the displacement reaches 0.265 mm, the force reaches the maximum value of 1188 N. Therefore, it can be concluded that the cohesive fracture model can accurately characterise the peak displacement and peak force of rocks during the SCB test.

Fig. 16 shows the numerically simulated positive stress in the distribution along the x-direction at the peak force. According to

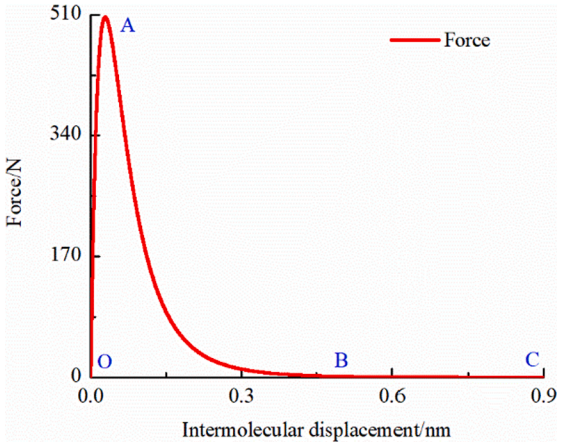

Fig. 13. Intermolecular displacement-tensile force curve.

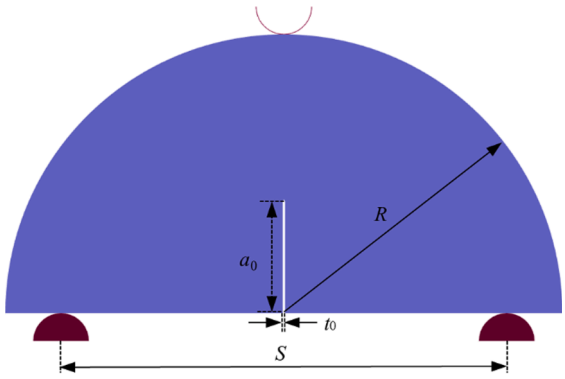

Fig. 14. Schematic of the SCB numerical model.

Table 2
Description of the basic notations.

Basic notation	Description	Value (mm)
R	specimen radius	37
S	distance between support points	59.2
a_0	initial crack length	14.8
t_0	initial crack width	0.3

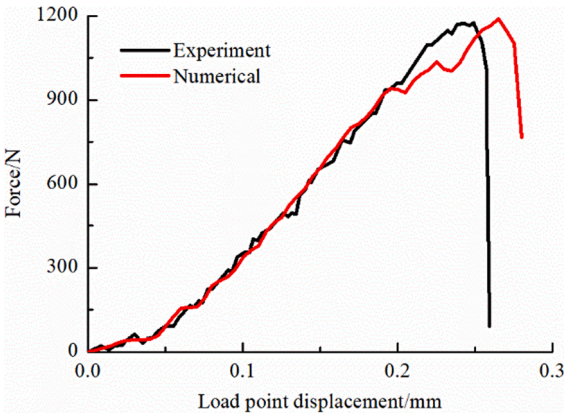

Fig. 15. Experimental and numerical displacement-force curve for SCB test.

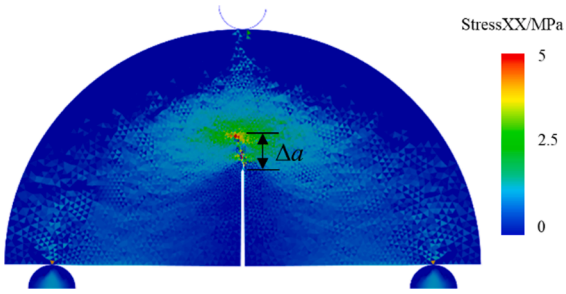

Fig. 16. Numerical simulated positive stress in the distribution along the x-direction.

Fig. 16, it can be concluded that the length Δa of the fracture process zone (FPZ) in the numerical simulation is 5.9 mm. Compared with the experimental value 8.5 mm, the error is 30.6%. Fig. 17 shows the numerically simulated displacement in the distribution along the x-direction after loading. It can be observed that the primary crack initiates from the notch tip because of the high stress concentration,

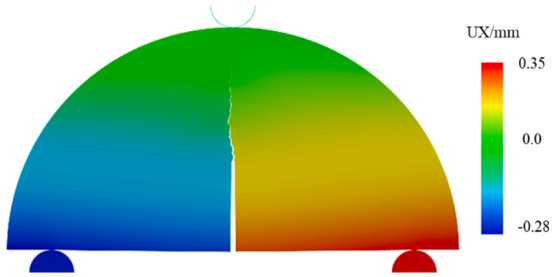

Fig. 17. Numerical simulated displacement in the distribution along the x-direction.

and subsequently, grows almost up to the symmetrical plane of the model. The propagation path of the primary crack is consistent with that concluded from the experimental results.

The accuracy of the cohesive fracture model for Mode-I test is verified based on the above numerical results.

4.2.2. Mode-II test

Numerical simulation of the Mode-II test is conducted to mainly confirm whether the cohesive fracture model can accurately characterise the shear fracture energy of rocks during the shear process. The Mode-II test is conducted on a square model with a dimension of 20 cm × 20 cm, and the numerical model is plotted in Fig. 18. It can be observed that there is a virtual interface (the dotted line in Fig. 18) in the middle of the numerical model. The linear elastic model is adopted as the constitutive model of the element, and the cohesive fracture model is adopted as the constitutive model of the virtual interface. The numerical simulation includes two stages. In the first stage, a vertical velocity, $v_y = 1 \times 10^{-8}$ m/s is applied at the top boundary, and the bottom boundary is fixed. In the second stage, initially, the vertical velocity v_y at the top boundary is reduced to zero, and the top boundary is fixed. Thereafter, a horizontal velocity $v_x = 1 \times 10^{-8}$ m/s is applied at the upper half of the left boundary, and the lower half of the right boundary is fixed. In the CDEM-based simulation of the Mode-II test, the mechanical parameters that must be provided as inputs include the mechanical parameters of the element and interface. Because the constitutive model of the element is the linear elastic model, the density, Young's modulus and Poisson's ratio are required as inputs to the model. For the interface, the tensile strength, tensile fracture energy and shear fracture energy need to be input to calculate the values of the thickness ratio β, space occupancy ratio ω and contact ratio λ. In addition, when the interface undergoes shear failure, the model experiences sliding friction. Because the sliding friction force in CDEM is calculated based on the Mohr-Coulomb criterion, the friction angle needs to be input to calculate the sliding friction force. The mechanical parameters are shown in Table 3, and the parameters in the table are the generalised values of rocks.

In the first stage, the entire model produces a compressive deformation under the action of the vertical velocity v_y, and no crack is observed to have appeared at the interface. In the second stage, with the increase in the horizontal shear displacement, the curve corresponding to the change in the crack ratio α is plotted in Fig. 19. The curve of the crack ratio α exhibits a three-stage characteristic, as shown in Fig. 19(a). In the OA range, the crack ratio α is always zero with the increase in the horizontal shear displacement. In the AB range, the crack ratio α increases sharply from 0 to 1 with the increase in the horizontal shear displacement. In the BC range, the

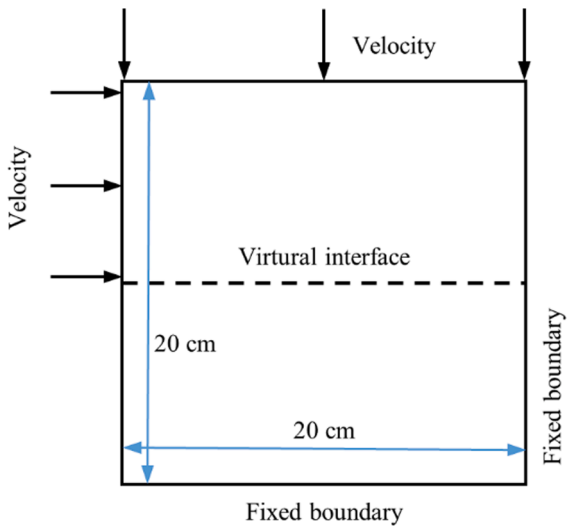

Fig. 18. Numerical model of Mode-II test.

Table 3
Mechanical parameters in Mode-II test.

Density (kg/m^3)	Young's modulus (GPa)	Poisson's ratio	Tensile strength (MPa)	Tensile fracture energy (J/m^2)	Shear fracture energy (J/m^2)	Friction angle (°)
2500	10	0.25	1	100	1000	35

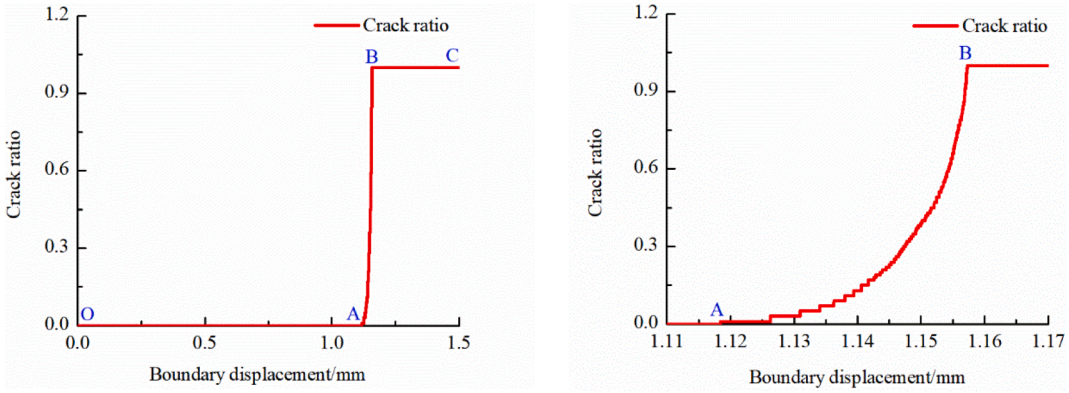

Fig. 19. Shear displacement-crack ratio α curve.

crack ratio α does not change, and it remains as 1. To more accurately obtain the changing trend of the crack ratio α, the shear displacement-crack ratio α curve in the AB range is plotted in Fig. 19(b). It can be observed that the crack ratio α increases nonlinearly from 0 to 1 with the increase in the shear displacement, and the increase rate gets accelerated.

To obtain the shear fracture energy, Fig. 20 plots the shear force curve corresponding to ID = 100 for the numerical spring (in the middle of interface) with the increase in the intermolecular shear displacement at the molecular scale. The curve exhibits an evident three-stage characteristic, and the area under the changing curves denotes the shear fracture energy. To obtain the shear fracture energy, the value of the area under the curve is first obtained by integration which represents only the value of the shear fracture energy at the molecular scale. Subsequently, the shear fracture energy at the particle scale is obtained based on the corresponding relation of the deformation at the molecular scale and particle scale; the numerical value of the spring shear fracture energy is calculated to be 0.5 J. Because the area represented by the numerical spring is 5×10^{-4} m^2, it can be concluded that the theoretical value of the shear fracture energy is 0.5 J under the premise that the shear fracture energy is 1000 J/m^2, and the numerical value is equal to the theoretical value.

To further evaluate the accuracy of the cohesive fracture model for the Mode-II test, the experimental results of the direct shear test conducted by Cho et al. [71] are adopted for a comparative analysis. The direct shear test is conducted on a cube with a dimension of 5 cm × 5 cm × 5 cm, and the numerical model is plotted in Fig. 21. The linear elastic model is adopted as the constitutive model of the element, and the cohesive fracture model is adopted as the constitutive model of the virtual interface. The numerical simulation includes two stages. In the first stage, a normal force F_y is applied at the top boundary, and the bottom boundary is fixed. In the second stage, a horizontal velocity $v_x = 1 \times 10^{-8}$ m/s is applied at the upper half of the left boundary, and the lower half of the right boundary is fixed. Based on the laboratory experiment, Cho et al. obtained the mechanical parameters. The density is 2630 kg/m^3, the Young's modulus is 2.5 GPa, the tensile strength is 2.6 MPa, the shear strength is 2.95 MPa and the friction angle is 39°.

In the direct shear test, a total of 11 samples were tested with the normal stress ranging from 1.0 kPa to 2.1 MPa. The experimental and numerical results are plotted in Fig. 22. It can be seen that the changing trends of the experimental and numerical results are consistent: with the increase in the normal stress, the shear stress gradually increases. The linear regression function is used to fit the experimental and numerical data; the fitting curve of numerical data is the green dotted line in Fig. 22, and the fitting curve of the experimental data is the blue dotted line in Fig. 22. The fitting function of the numerical data is given by

$$\sigma_s = 0.70\sigma_n + 2.58 \tag{47}$$

The fitting function of experimental data is given by

$$\sigma_s = 0.80\sigma_n + 2.81 \tag{48}$$

Based on the fitting curve of the numerical data, it can be concluded that the friction angle is 35°, and the cohesive strength is 2.58 MPa. Based on the fitting curve of the experimental data, it can be concluded that the friction angle is 38.8°, and the cohesive strength is 2.81 MPa. The error of the friction angle is 9.79%, and the error of the cohesive strength is 8.19%. The errors of the friction angle and cohesive strength are all less than 10%, indicating the accuracy of the new cohesive fracture model corresponding to the Mode-II test.

The accuracy of the cohesive fracture model for Mode-II test is verified based on the above numerical results.

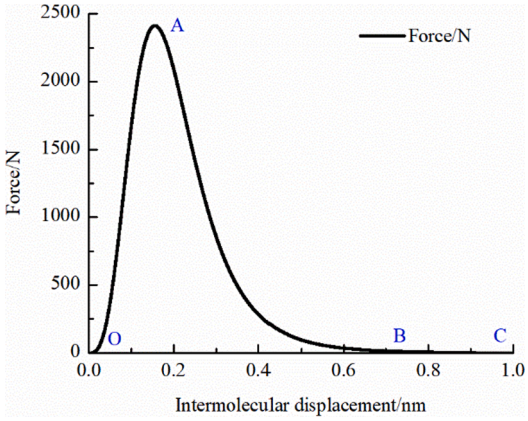

Fig. 20. Intermolecular shear displacement-shear force curve.

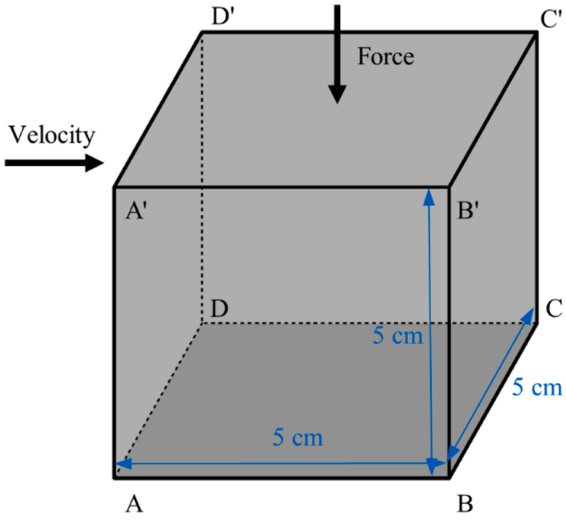

Fig. 21. Numerical model of the direct shear test [71].

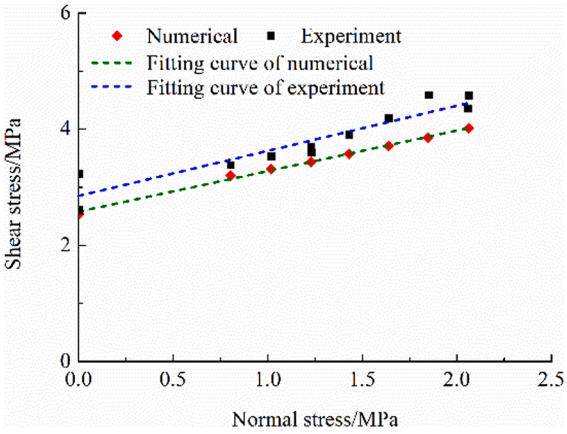

Fig. 22. Normal stress-shear stress curve of direct shear test.

4.2.3. Uniaxial compression test

To further study the accuracy of the novel cohesive fracture model, the numerical simulation of rock uniaxial compression test is conducted. Kazerani conducted the uniaxial compression laboratory test of the Transjurane sandstone, and the stress-strain curve and the related mechanical parameters were obtained [72]. The 3D numerical model of the transjurane sandstone are represented in Fig. 23, illustrating a cylinder with a dimension of 8 cm × 16 cm. A vertical velocity $v_y = 2 \times 10^{-8}$ m/s is applied at the top boundary, and the bottom boundary is fixed. The numerical model is discretised into a series of tetrahedral elements, and the common boundary of the elements is set as the virtual interface. The linear elastic model is adopted as the constitutive model of the element, and the cohesive fracture model is adopted as the constitutive model of the virtual interface. The mechanical parameters of the transjurane sandstone are shown in Table 4, and the value of the fracture energy is quoted from the laboratory test of the transjurane sandstone. Kazerani conducted a wide range of experimental investigations on the transjurane sandstone in the rock mechanics laboratory of the Swiss Federal Institute of Technology, and the average standard mechanical properties (for example, Young's modulus, fracture toughness in Mode-I and fracture toughness in Mode-II) are obtained. Jiang et al. calculated the Mode-I fracture energy G_{fI} and Mode-II fracture energy G_{fII} of the transjurane sandstone based on the experimental results, and the values of the G_{fI} and G_{fII} are adopted for numerical simulation of the uniaxial compression test.

The accuracy of the cohesive fracture model in simulating the rock fracture process is analysed by comparing the stress-strain curve and fracture pattern obtained by the laboratory test and numerical simulation.

A comparison of the numerical and experimental axial strain-compressive stress relationship in the uniaxial compression test is plotted in Fig. 24. It can be observed that the changing trends of the curves are similar. Before the axial strain of the rock reaches the peak strain, with the increase in the axial strain, the compressive stress gradually increases. Once the axial strain reaches the peak strain, the compressive stress decreases rapidly. The values of the peak compressive stress and peak axial strain in the laboratory test and numerical simulation are similar. In the laboratory test, when the axial strain reaches 4.05%, the compressive stress reaches the maximum value of 40.0 MPa. In the numerical simulation, when the axial strain reaches 4.30%, the compressive stress reaches the maximum value of 39.2 MPa. Therefore, it can be concluded that the cohesive fracture model can accurately characterise the peak strain and peak stress of the rock in the uniaxial compression test.

The rock fracture patterns obtained by numerical simulation and laboratory test are plotted in Fig. 25. It can be observed that the rock specimen has an obvious oblique fracture plane in the laboratory test, as shown in Fig. 25(a), and the numerical model also has an obvious oblique fracture plane in the numerical simulation, as shown in Fig. 25(b). In addition, the angles of the oblique fracture plane in the numerical simulation and laboratory test are similar. Because the oblique main fracture plane in the laboratory test is captured in the numerical simulation, it can be concluded that the main fracture pattern of the laboratory test is the same as that in the numerical simulation.

To evaluate the influence of the mesh on the numerical results and the proposed model, the numerical model in Fig. 23 is divided by tetrahedral elements of different sizes (6 mm, 7 mm, 8 mm, 9 mm and 10 mm), and the variation of the numerical results for different cases of the mesh division are studied. The element number at different mesh sizes is shown in Table 5, and it can be observed that the element number for a mesh size of 6 mm is almost 4.2 times than that for a mesh size of 10 mm.

The peak stress calculated for different element numbers is plotted in Fig. 26. It can be observed that with the increase in the element number, the peak stress does not increase or decrease significantly which is basically consistent with the experimental result. In the five mesh cases, the maximum peak stress obtained by numerical simulation is 41.61 MPa, the corresponding element number being 14851, and the minimum peak stress obtained by numerical simulation is 39.17 MPa, the corresponding element number being 4765. Compared with the experimental result 40.03 MPa, the error is approximately in the range of −2.15% to 3.97%. When the model

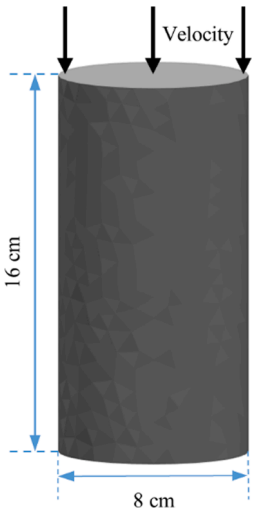

Fig. 23. 3D numerical model of transjurane sandstone.

Table 4
Mechanical parameters of transjurane sandstone.

Density (kg/m^3)	Young's modulus (GPa)	Tensile strength (MPa)	Friction angle (°)	Tensile fracture energy (J/m^2)	Shear fracture energy (J/m^2)
2500	12.5	2.8	41	50	150

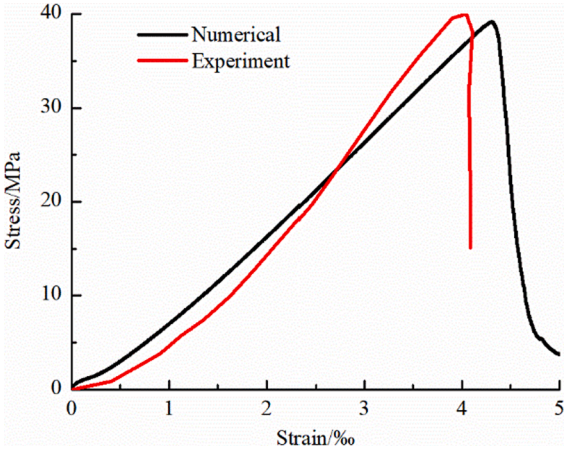

Fig. 24. Axial strain-compressive stress curve.

(a) Laboratory test (b) Numerical simulation

Fig. 25. Fracture pattern of rock in the laboratory test and numerical simulation.

Table 5
Number of elements.

	Element size (mm)				
	6	7	8	9	10
Number of elements	14,851	9190	6512	4765	3550

enters the post-peak stage, the vertical displacement nephograms for the different element numbers are plotted in Fig. 27. It can be seen that the fracture patterns of the model are basically the same: there is a main fracture surface, and the inclination angle of the fracture surface is similar. Based on the analysis of the peak stress and fracture patterns for the different element numbers, it can be concluded that the mesh has negligible influences on the numerical results and proposed model.

Based on the numerical results of Mode-I test, Mode-II test and uniaxial compression test, it can be concluded that the cohesive fracture model can appropriately simulate the complex fracture process of rocks.

5. Conclusions

This study proposed a novel cohesive fracture model based on the multi-scale model of rocks and Lennard-Jones potential to

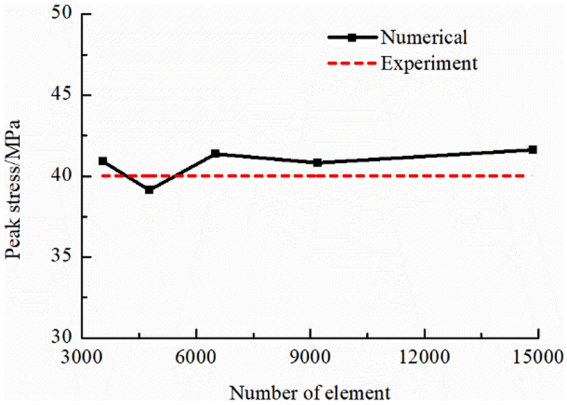

Fig. 26. Peak stress for different element numbers.

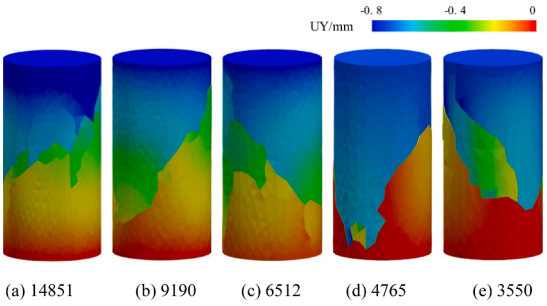

Fig. 27. Vertical displacement nephograms for different element numbers.

investigate the energy dissipation phenomenon of rocks. First, the multi-scale model of rocks and several key parameters were proposed. Thereafter, the force and potential energy equations of the cohesive fracture model were established. Finally, the accuracy of cohesive fracture model was studied based on three numerical simulations. The following conclusions can be drawn:

(1) In the multi-scale model of the rock, the increase in distance between mineral particles at the particle scale is equal to the strain at the RVE scale multiplied by the initial distance between the mineral particles. In addition, the increase in the distance between the mineral particles at the particle scale is equal to the cumulative value of the increase in the intermolecular distance at the molecular scale.
(2) The rock changes from continuous medium to discontinuous medium during the initiation and propagation process of cracks, and the underlying mechanism of the fracture energy is represented by the transformation of a portion of the deformation energy of the continuous field into the potential energy between molecules in the rupture field.
(3) Based on the numerical results of the Mode-I and Mode-II tests, it can be determined that the cohesive fracture model can fit both the theoretical values as well as the experimental results. Based on the numerical results of the uniaxial compression test, it can be concluded that the cohesive fracture model can accurately simulate the uniaxial compressive strength and fracture pattern of rocks.

6. Data availability statement

Data in this manuscript is good to offer, is there is any request, please contact Corresponding Author.

Declaration of Competing Interest

The authors declare that they have no known competing financial interests or personal relationships that could have appeared to influence the work reported in this paper.

Acknowledgements

The authors would like to acknowledge the financial support of the National Key Research and Development Project of China, the Ministry of Science and Technology of China (Project No. 2018YFC1505504).

References

[1] Salvoni M, Dight PM. Rock damage assessment in a large unstable slope from microseismic monitoring - MMG Century mine (Queensland, Australia) case study. Engng Geol 2016;210:45–56.
[2] Ma Q, Tan Y, Liu X, Gu Q, Li X. Effect of coal thicknesses on energy evolution characteristics of roof rock-coal-floor rock sandwich composite structure and its damage constitutive model. Compos B Engng 2020;198:108086.
[3] Zheng H, Li T, Shen J, Xu C, Sun H, Lü Q. The effects of blast damage zone thickness on rock slope stability. Engng Geol 2018;246:19–27.
[4] Ma K, Liu G, Guo L, Zhuang D, Collins DS. Deformation and stability of a discontinuity-controlled rock slope at Dagangshan hydropower station using three-dimensional discontinuous deformation analysis. Int J Rock Mech Min Sci 2020;130:104313.
[5] Han H, Fukuda D, Liu H, Fathi Salmi E, Sellers E, Liu T, et al. FDEM simulation of rock damage evolution induced by contour blasting in the bench of tunnel at deep depth. Tunn Undergr Space Technol 2020;103:103495.
[6] Liu H, Yuan X, Xie T. A damage model for frost heaving pressure in circular rock tunnel under freezing-thawing cycles. Tunn Undergr Space Technol 2019;83:401–8.
[7] Vazaios I, Vlachopoulos N, Diederichs MS. Assessing fracturing mechanisms and evolution of excavation damaged zone of tunnels in interlocked rock masses at high stresses using a finite-discrete element approach. J Rock Mech Geotech Engng 2019;11:701–22.
[8] He T-M, Zhao Q, Ha J, Xia K, Grasselli G. Understanding progressive rock failure and associated seismicity using ultrasonic tomography and numerical simulation. Tunn Undergr Space Technol 2018;81:26–34.
[9] Tang Y, Okubo S, Xu J, Peng S. Progressive failure behaviors and crack evolution of rocks under triaxial compression by 3D digital image correlation. Engng Geol 2019;249:172–85.
[10] Yang S-Q, Chen M, Huang Y-H, Jing H-W, Ranjith PG. An experimental study on fracture evolution mechanism of a non-persistent jointed rock mass with various anchorage effects by DSCM, AE and X-ray CT observations. Int J Rock Mech Min Sci 2020;134:104469.
[11] Du K, Li X, Tao M, Wang S. Experimental study on acoustic emission (AE) characteristics and crack classification during rock fracture in several basic lab tests. Int J Rock Mech Min Sci 2020;133:104411.
[12] Wang Y, Feng WK, Wang HJ, Li CH, Hou ZQ. Rock bridge fracturing characteristics in granite induced by freeze-thaw and uniaxial deformation revealed by AE monitoring and post-test CT scanning. Cold Reg Sci Technol 2020;177:103115.
[13] Zhang Z, Wang E, Li N. Fractal characteristics of acoustic emission events based on single-link cluster method during uniaxial loading of rock. Chaos, Solitons Fractals 2017;104:298–306.
[14] Liang Y, Li Q, Gu Y, Zou Q. Mechanical and acoustic emission characteristics of rock: effect of loading and unloading confining pressure at the postpeak stage. J Nat Gas Sci Engng 2017;44:54–64.
[15] Lin Q, Mao D, Wang S, Li S. The influences of mode II loading on fracture process in rock using acoustic emission energy. Engng Fract Mech 2018;194:136–44.
[16] Li G, Tang C-A. A statistical meso-damage mechanical method for modeling trans-scale progressive failure process of rock. Int J Rock Mech Min Sci 2015;74:133–50.
[17] Fang W, Jiang N, Luo X. Establishment of damage statistical constitutive model of loaded rock and method for determining its parameters under freeze-thaw condition. Cold Reg Sci Technol 2019;160:31–8.
[18] Huang S, Liu Q, Cheng A, Liu Y. A statistical damage constitutive model under freeze-thaw and loading for rock and its engineering application. Cold Reg Sci Technol 2018;145:142–50.
[19] Wang Z-L, Li Y-C, Wang JG. A damage-softening statistical constitutive model considering rock residual strength. Comput Geosci 2007;33:1–9.
[20] Gao W, Chen X, Hu C, Zhou C, Cui S. New damage evolution model of rock material. Appl Math Model 2020;86:207–24.
[21] Geng Q, Wei Z, Ren J. New rock material definition strategy for FEM simulation of the rock cutting process by TBM disc cutters. Tunn Undergr Space Technol 2017;65:179–86.
[22] Chiang LE, Elías DA. A 3D FEM methodology for simulating the impact in rock-drilling hammers. Int J Rock Mech Min Sci 2008;45:701–11.
[23] Hatzigeorgiou GD, Beskos DE. Static analysis of 3D damaged solids and structures by BEM. Engng Anal Boundary Elem 2002;26:521–6.
[24] Liu CL, Li G, Kuriyama K, Mizuta Y. Development of a computer program for inhomogeneous modeling using 3-D BEM with analytical integration and its application to rock slope stability evaluation. Int J Rock Mech Min Sci 2005;42:137–44.
[25] Maryška J, Severýn O, Tauchman M, Tondr D. Modelling of processes in fractured rock using FEM/FVM on multidimensional domains. J Comput Appl Math 2008;215:495–502.
[26] Shen B, Shi J. A numerical scheme of coupling of fluid flow with three-dimensional fracture propagation. Engng Anal Boundary Elem 2019;106:243–51.
[27] Zhang Y, Zhuang X. Cracking elements: a self-propagating Strong Discontinuity embedded Approach for quasi-brittle fracture. Finite Elem Anal Des 2018;144:84–100.
[28] Zhang Y, Zhuang X. Cracking elements method for dynamic brittle fracture. Theor Appl Fract Mech 2019;102:1–9.
[29] Mu L, Zhang Y. Cracking elements method with 6-node triangular element. Finite Elem Anal Des 2020;177:103421.
[30] Han F, Lubineau G, Azdoud Y. Adaptive coupling between damage mechanics and peridynamics: a route for objective simulation of material degradation up to complete failure. J Mech Phys Solids 2016;94:453–72.
[31] Han F, Lubineau G, Azdoud Y, Askari A. A morphing approach to couple state-based peridynamics with classical continuum mechanics. Comput Methods Appl Mech Engng 2016;301:336–58.
[32] Rokkam S, Gunzburger M, Brothers M, Phan N, Goel K. A nonlocal peridynamics modeling approach for corrosion damage and crack propagation. Theor Appl Fract Mech 2019;101:373–87.
[33] Regassa B, Xu N, Mei G. An equivalent discontinuous modeling method of jointed rock masses for DEM simulation of mining-induced rock movements. Int J Rock Mech Min Sci 2018;108:1–14.
[34] Che N, Wang H, Jiang M. DEM investigation of rock/bolt mechanical behaviour in pull-out tests. Particuology. 2020;52:10–27.
[35] Gu DM, Huang D, Zhang WG, Gao XC, Yang C. A 2D DEM-based approach for modeling water-induced degradation of carbonate rock. Int J Rock Mech Min Sci 2020;126:104188.
[36] Rezanezhad M, Lajevardi SA, Karimpouli S. Effects of pore-crack relative location on crack propagation in porous media using XFEM method. Theor Appl Fract Mech 2019;103:102241.
[37] Haeri H, Sarfarazi V, Ebneabbasi P, Nazari Maram A, Shahbazian A, Fatehi Marji M, et al. XFEM and experimental simulation of failure mechanism of non-persistent joints in mortar under compression. Constr Build Mater 2020;236:117500.
[38] Tsesarsky M, Hatzor YH. Tunnel roof deflection in blocky rock masses as a function of joint spacing and friction – a parametric study using discontinuous deformation analysis (DDA). Tunn Undergr Space Technol 2006;21:29–45.
[39] Ni K, Yang J, Ning Y, Kang G. A modified sub-block DDA fracturing modelling method for rock. Engng Anal Boundary Elem 2020;111:154–66.
[40] Wu Q, An Y, Liu Q-Q. SPH-based simulations for slope failure considering soil-rock interaction. Procedia Engng 2015;102:1842–9.
[41] Wang Y, Bui HH, Nguyen GD, Ranjith PG. A new SPH-based continuum framework with an embedded fracture process zone for modelling rock fracture. Int J Solids Struct 2019;159:40–57.
[42] Zhai SF, Zhou XP, Bi J, Xiao N. The effects of joints on rock fragmentation by TBM cutters using General Particle Dynamics. 2016;57:162-72.
[43] Li Z, Shou Y, Zhang X, Chen L, Berto F. Stability analysis of flawed rock slope by using virtual-bond-based general particles dynamics. Theor Appl Fract Mech 2020;108:102631.
[44] Ai W, Augarde CE. Thermoelastic fracture modelling in 2D by an adaptive cracking particle method without enrichment functions. Int J Mech Sci 2019;160:343–57.
[45] Ai W, Bird RE, Coombs WM, Augarde CE. A configurational force driven cracking particle method for modelling crack propagation in 2D. Engng Anal Boundary Elem 2019;104:197–208.

[46] Xiao N, Zhou X-P, Gong Q-M. The modelling of rock breakage process by TBM rolling cutters using 3D FEM-SPH coupled method. Tunn Undergr Space Technol 2017;61:90–103.
[47] Zárate F, Gonzalez JM, Miquel J, Löhner R, Oñate E. A coupled fluid FEM-DEM technique for predicting blasting operations in tunnels. Underground Space 2018;3:310–6.
[48] Wu Z, Yu F, Zhang P, Liu X. Micro-mechanism study on rock breaking behavior under water jet impact using coupled SPH-FEM/DEM method with Voronoi grains. Engng Anal Boundary Elem 2019;108:472–83.
[49] Wu Z, Zhang P, Fan L, Liu Q. Numerical study of the effect of confining pressure on the rock breakage efficiency and fragment size distribution of a TBM cutter using a coupled FEM-DEM method. Tunn Undergr Space Technol 2019;88:260–75.
[50] Jiang H, Zhao H, Gao K, Wang O, Wang Y, Meng D. Numerical investigation of hard rock breakage by high-pressure water jet assisted indenter impact using the coupled SPH/FEM method. Powder Technol 2020.
[51] JianPing Y, WeiZhong C, DianSen Y, JingQiang Y. Numerical determination of strength and deformability of fractured rock mass by FEM modeling. Comput Geotech 2015;64:20–31.
[52] Xu H, Wang G, Fan C, Liu X, Wu M. Grain-scale reconstruction and simulation of coal mechanical deformation and failure behaviors using combined SEM Digital Rock data and DEM simulator. Powder Technol 2020;360:1305–20.
[53] Mardalizad A, Saksala T, Manes A, Giglio M. Numerical modeling of the tool-rock penetration process using FEM coupled with SPH technique. J Petrol Sci Engng 2020;189:107008.
[54] Han W, Jiang Y, Luan H, Du Y, Zhu Y, Liu J. Numerical investigation on the shear behavior of rock-like materials containing fissure-holes with FEM-CZM method. Comput Geotech 2020;125:103670.
[55] Barenblatt GI. The formation of equilibrium cracks during brittle fracture. General ideas and hypotheses. Axially-symmetric cracks. J Appl Math Mech 1959;23:622–36.
[56] Dugdale DS. Yielding of steel sheets containing slits. J Mech Phys Solids 1960;8:100–4.
[57] Hillerborg A, Modéer M, Petersson PE. Analysis of crack formation and crack growth in concrete by means of fracture mechanics and finite elements. Cem Concr Res 1976;6:773–81.
[58] Alfano G. On the influence of the shape of the interface law on the application of cohesive-zone models. Compos Sci Technol 2006;66:723–30.
[59] Gálvez JC, Červenka J, Cendón DA, Saouma V. A discrete crack approach to normal/shear cracking of concrete. Cem Concr Res 2002;32:1567–85.
[60] Yang ZJ, Su XT, Chen JF, Liu GH. Monte Carlo simulation of complex cohesive fracture in random heterogeneous quasi-brittle materials. Int J Solids Struct 2009;46:3222–34.
[61] Wu Z, Liang X, Liu Q. Numerical investigation of rock heterogeneity effect on rock dynamic strength and failure process using cohesive fracture model. Engng Geol 2015;197:198–210.
[62] Zhou W, Tang L, Liu X, Ma G, Chen M. Mesoscopic simulation of the dynamic tensile behaviour of concrete based on a rate-dependent cohesive model. Int J Impact Engng 2016;95:165–75.
[63] Gui Y, Bui HH, Kodikara J. An application of a cohesive fracture model combining compression, tension and shear in soft rocks. Comput Geotech 2015;66:142–57.
[64] Jiang H, Meng D. 3D numerical modelling of rock fracture with a hybrid finite and cohesive element method. Engng Fract Mech 2018;199:280–93.
[65] Nguyen NHT, Bui HH, Nguyen GD, Kodikara J. A cohesive damage-plasticity model for DEM and its application for numerical investigation of soft rock fracture properties. Int J Plast 2017;98:175–96.
[66] Whittles DN, Kingman S, Lowndes I, Jackson K. Laboratory and numerical investigation into the characteristics of rock fragmentation. Miner Engng 2006;19:1418–29.
[67] Ju Y, Liu P, Chen J, Yang Y, Ranjith PG. CDEM-based analysis of the 3D initiation and propagation of hydrofracturing cracks in heterogeneous glutenites. J Nat Gas Sci Engng 2016;35:614–23.
[68] Wang H, Bai C, Feng C, Xue K, Zhu X. An efficient CDEM-based method to calculate full-scale fragment field of warhead. Int J Impact Engng 2019;133:103331.
[69] Feng C, Li S, Liu X, Zhang Y. A semi-spring and semi-edge combined contact model in CDEM and its application to analysis of Jiweishan landslide. J Rock Mech Geotech Engng 2014;6:26–35.
[70] Wei MD, Dai F, Xu NW, Zhao T, Xia KW. Experimental and numerical study on the fracture process zone and fracture toughness determination for ISRM-suggested semi-circular bend rock specimen. Engng Fract Mech 2016;154:43–56.
[71] Cho N, Martin CD, Sego DC. Development of a shear zone in brittle rock subjected to direct shear. Int J Rock Mech Min Sci 2008;45:1335–46.
[72] Kazerani T. Effect of micromechanical parameters of microstructure on compressive and tensile failure process of rock. Int J Rock Mech Min Sci 2013;64:44–55.